Shock-vortex shear-layer interaction in the transonic flow around a supercritical airfoil at high Reynolds number in buffet conditions

Damien Szubert, Fernando Grossi, Antonio Jimenez Garcia, Yannick Hoarau, Julian Charles Roland Hunt, Marianna Braza

Shock-vortex shear-layer interaction in the transonic flow around a supercritical airfoil at high Reynolds number in buffet conditions

Damien Szubert [a,*], Fernando Grossi [a], Antonio Jimenez Garcia [a], Yannick Hoarau [b], Julian C.R. Hunt [c], Marianna Braza [a]

[a] Institut de Mécanique des Fluides de Toulouse, UMR No 5502 CNRS-INPT-UPS, Allée du Prof. Camille Soula, F-31400 Toulouse, France
[b] Laboratoire ICUBE, UMR No 7357, Strasbourg, France
[c] Department of Earth Sciences, University College London, London WC1E 6BT, UK

ARTICLE INFO

Keywords:
Transonic flow
Buffet instabilities
Wavelets
POD
Turbulence modelling
Stochastic forcing

ABSTRACT

This paper provides a conceptual analysis and a computational model for how the unsteady 'buffeting' phenomenon develops in transonic, low incidence flow around a supercritical aerofoil, the OAT15A, at Reynolds number of 3.3 million. It is shown how a low-frequency buffet mode is amplified in the shock-wave region and then develops upstream and downstream interaction with the alternating von Kármán eddies in the wake past the trailing-edge as well as with the shear-layer, Kelvin–Helmholtz vortices. These interactions are tracked by wavelet analysis, autoregressive (AR) modelling and by Proper Orthogonal Decomposition. The frequency modulation of the trailing-edge instability modes is shown in the spectra and in the wall-pressure fluctuations. The amplitude modulation of the buffet and von Kármán modes has been also quantified by POD analysis. The thinning of the shear layers, both at the outer edge of the turbulent boundary layers and the wake, caused by an 'eddy-blocking' mechanism is modelled by stochastic forcing of the turbulent kinetic energy and dissipation, by small-scale straining of the higher-order POD modes. The benefits from thinning the shear-layers by taking into account the interfacial dynamics are clearly shown in the velocity profiles, and wall pressure distribution in comparison with the experimental data.

1. Introduction

Understanding the various mechanisms related to buffet instabilities in the transonic flow around a supercritical airfoil is the main objective of this paper. A detailed physical analysis is developed for the interactions between shock waves and the boundary layer over the aerofoil, as well as between wake vortices and the shock waves. A further complexity arises from the interactions between the wake vortices near the trailing edge and the fluctuating sheared interface that bounds the wake flow. Pioneering studies of Levy (1978) and Seegmiller et al. (1978), made evidence of a shock unsteadiness characterised by a low-frequency and high-amplitude, in the Mach number range 0.7–0.8 corresponding to aircraft's cruise-speed. Several experimental

* Corresponding author.

and numerical studies have been devoted to this flow phenomenon and its impact on the aerodynamic forces: McDevitt et al. (1976), Jacquin et al. (2005, 2009) and Brunet (2003).

Whereas the majority of the studies devoted to the transonic interaction deal with the high-Reynolds number range, the physical mechanisms of the buffet onset can be studied more easily in the lower Reynolds number range, allowing for Direct Numerical Simulation. For a NACA0012 airfoil, (Bouhadji and Braza, 2003a, 2003b) have analysed the successive states of the unsteadiness due to the compressibility effects in the Mach number range 0.3–1.0 by 2D and 3D Navier–Stokes simulations. The buffet instability was analysed in association with the von Kármán vortex shedding in the Mach number range 0.75–0.85, as well as the suppression of the buffet form Mach numbers beyond 0.85. The buffet mode has also been analysed by DNS of Bourdet et al. (2003), who used in addition the Stuart-Landau model (Landau, 1944) in order to quantify the linear and non-linear parts of the buffet instability.

These studies showed the sharp rise of the drag coefficient as the Mach number increases in the range 0.7–0.8, as well as the interaction of the shock wave with the von Kármán wake instability downstream of the trailing-edge. It was shown that this instability was formed in the wake and propagated towards the trailing-edge beyond a low-subsonic critical value of the Mach number, of order 0.2, for a NACA0012 airfoil at zero incidence and Reynolds number of 10 000 (Bouhadji, 1998). This instability (mode I) persists within the whole transonic speed interval, up to Mach number of order 0.85, independently on the appearance of the buffet. This second instability (mode II) was found to appear in the interval 0.75–0.8 and to strongly interact with mode I, where the buffet was sustained by mode I. Experimental evidence of mode I was made by the Schlieren visualisations of D.W. Holder (Fung, 2002), Fig. 7.

Numerical simulations in the high-Re range (Grossi et al., 2012b; Jimenez-Garcia, 2012), regarding a supercritical airfoil, the OAT15A, introduced a splitter-plate at the trailing edge, which suppressed the von Kármán mode. It was shown that in the cases where the von Kármán mode was remote (downstream of a critical length of the splitter plate), the buffet mode was considerably attenuated and disappeared. Therefore, it is worthwhile analysing the interaction of these two modes in the high-Reynolds number regimes for aerodynamics applications. In particular, there is little knowledge of this kind of interaction in the state of the art with regard to the high-Re range as well as more generally, of the trailing-edge dynamics feedback effect towards the shock-wave/boundary-layer interaction region (SWBLI) upstream of the trailing-edge. Lee (1990) reported a schematic explanation of the buffet interaction with Kutta waves coming from the trailing-edge, without a quantification of this interaction. Furthermore, it is worthwhile mentioning that the SWBLI is followed by separation of the boundary layer and by the formation of *thin* shear layers at the edges of the boundary layers and in the wake, where local Kelvin–Helmholtz (K–H) instabilities are observed.

In order to compute the interactions and feedback between the shear-layer and trailing-edge instabilities with the upwind shock-buffet mode, new methods are needed. These have to overcome the tendency of the shear layers to thicken downstream of the SWBLI, because of the turbulent shear stress modelling near the interface is usually approximated by employing eddy-viscosity concepts based on equilibrium turbulence hypotheses and direct cascade. In the flow physics however, upscale phenomena occur that increase the energy of the turbulence spectrum from intermediate range towards the lower wavenumbers (Braza et al., 2006). These mechanisms are not yet sufficiently taken into account in the modelling equations. However, theoretical analysis (Hunt et al., 2008) and experimental studies (e.g. Ishihara et al., 2015) show that these stresses are generated by the inhomogeneous small-scale motions in the turbulent region near the interface and thence increase the local "conditional" shear and "eddy blocking effect" within the interfacial layer (Fig. 1). This influence of small scales on the whole flow is effectively an "upscale" process. The local turbulence adjacent to the interface tends to reduce the Kelvin–Helmholtz instability modes of the interface (Dritschel et al., 1991).

A new approach for modelling the interface regions is needed, which can be based on recent numerical and experimental research into turbulent interfacial shear flows, on the outer edges of jets, wakes and the outer parts of boundary layers with thickness L. The thin randomly moving interfaces which separate regions of strong and weak turbulence have a thickness $\ell(\ll L)$. This general property of turbulent flows was in fact suggested and discussed by Prandtl in 1905, though he did not take it further once he became interested in the mixing length model of the mean properties of turbulent shear flows (see Bodenschatz and Eckert, 2011; Taveira and da Silva, 2014). Within these layers, the average shear (or in 2-dimensions the gradient of shear) is much stronger than that in the adjacent turbulent shear flows. At very high Reynolds numbers Re, determined by L and the *R.M.S.*, turbulent velocity u_o, the thickness ℓ of these interface layers is of the order of the Taylor microscale ℓ_v (i.e $L\,\mathrm{Re}^{-1/2}$), but within them very thin elongated vortices form with a thickness ℓ_v of the order of the Kolmogorov microscale (i.e. $\ell_v \sim L\,\mathrm{Re}^{-3/4}$, Eames and Flor, 2011). Numerical simulations show that these sharp interfaces occur even in complex turbulent flows, such as flows over aircraft wings (Braza, 2011).

These interfaces have their own mean local dynamics that keep the mean gradients at the interface at a maximum, through eddy blocking and enhanced vortex stretching (Hunt et al., 2008). Similar bounding interfaces also occur at the edges of patches of turbulence, such as puffs or vortex rings (Holzner et al., 2008). These intensely sheared layers interact with the motions outside the layers by blocking external eddies (through shear sheltering), which leads to a balance between sharpening of the velocity gradients in the layer and the tendency to diffuse outwards (Hunt et al., 2008). The typical spacing between the interfacial layers is of order of the "dissipation integral length scale" (Hunt et al., 2014).

Thus, the overall high-Re dynamics of the interface has to be modelled in order to correctly represent the turbulent transfers through the rotational–irrotational regions either side of these interfaces that have to be kept thin. This modelling has to include the complex interactions between the developing instability modes and the fine-scale turbulence. It is necessary to have a comprehensive turbulence model that should include the effects of the low-frequency organized motion

and the transfers due to the random turbulence. Such models should take sufficient account of the large and small motion effects, especially the shear–stress gradients as studied at high-Re atmospheric flows by Hunt et al. (1984). The turbulence modelling in the present case should also accurately predict the pressure distribution and the unsteady loads in fluid–structure interaction.

In this context, approaches such as standard URANS, derived from assumptions of turbulence in statistical equilibrium and using downscale cascade, tend to produce higher rates of the turbulence kinetic energy and to underestimate the global coefficients (drag, lift) and their amplitudes (Haase et al., 2009).

The Large Eddy Simulation uses a number of degrees of freedom being orders of magnitude higher than the grid size needed for URANS and hybrid approaches. For moderate Reynolds number flows (Re $O(10^4)$), LES can capture the major instabilities past bodies, whereas for the high-Reynolds number range (Re $> 10^6$), for industrial designs, it is not practical with typical computational capacity to apply LES for aerodynamic flows around lifting structures. Furthermore, even with LES methods, improvements can be expected by reconsidering the classical downscale energy transfer models for the small-scale eddies in the dissipative wave-number range by using upscale transfer processes in the turbulence modelling of the thin interfaces.

Recent efforts in turbulence modelling are devoted to accurately reproduce the flow physics in respect of instability amplification, strong flow detachment and accurate prediction of the associated frequencies, unsteady loads and in particular, of pressure fluctuations, representing a crucial need for aeroacoustics.

Hybrid RANS-LES methods are quite suitable for this category of *fluid–structure interaction* problems, because they associate the benefits of URANS in the near-region and those of LES in the regions of flow detachment, as reported the proceedings of the 4th HRLM, 'Hybrid RANS-LES Methods' symposium (Fu et al., 2012). Hybrid methods can be considerably improved by using adapted URANS modelling in the near-wall region and adapted LES modelling in the flow detachment areas, in order to allow for modification of the turbulent scales accounting for non-equilibrium turbulence.

In this context, improved URANS approaches can be used to reduce the turbulent viscosity levels and allow the amplification of instabilities, as for example the Scale Adaptive Simulation (SAS; Menter and Kuntz, 2003; Menter and Egorov, 2005), the Organised Eddy Simulation (OES; Braza et al., 2006; Bourguet et al., 2008, among others). SAS adapts the Kolmogorov turbulence scale according to flow regions governed by non-equilibrium turbulence effects. OES accounts for stress-strain directional misalignment in non-equilibrium turbulence regions thanks to a tensorial eddy-viscosity concept derived from Differential Reynolds Stress Modelling (DRSM) projection on the principal directions of the strain-rate tensor.

Although significant conceptual progress has been accomplished in the last decade, there still remain open questions with regard to the quantitative prediction of the above mechanisms with the accuracy required by the design. To our knowledge, the majority of the available modelling approaches produce less thin shear-layer interfaces, even by using considerably fine grids. This is generally due to a higher turbulence diffusion level than in the physical reality, produced by the modelling approaches, which mostly employ downstream turbulence cascade assumptions. In the present paper, the motivation is to enhance the eddy-blocking effect and vortex stretching in the sense of an upscale cascade.

On view of the above elements, the objectives of the present paper are as follows: to analyse in detail the interaction between two main instabilities, the buffet and the von Kármán modes in the transonic flow around a supercritical airfoil, whose configuration is involved in the next generation of civil aircraft design, by means of numerical simulation and adapted turbulence modelling concepts. A method of stochastic, *inhomogeneous* forcing of the turbulence transport equations is presented. This models the thin turbulent/non-turbulent, shear-layer interfaces and thence the large-scale flow structure on the purpose to provide the correct pressure fluctuations needed for fluid–structure interaction. The content of the following sections are as follows: Section 2 presents the flow configuration and the numerical approach. Section 3 presents the results regarding the buffet instability, its interaction with the shear-layer and near-wake instabilities based on conventional URANS/OES methods. This section includes in particular wavelet analysis and Proper Orthogonal Decomposition. In Section 4, the stochastic forcing approach for the higher modes is presented and compared with other methods and experimental results. Section 5 is the conclusion of the paper.

2. Flow configuration, numerical method and turbulence modelling

2.1. Test case description

The transonic buffet over the OAT15A airfoil was investigated in the experimental work by Jacquin et al. (2005, 2009), as well as by Brunet et al. (2003), by means of both experimental and numerical study at free-stream Mach numbers in the range of 0.70–0.75 and a chord-based Reynolds number of 3 million. The OAT15A is a supercritical wing section with a thickness-to-chord ratio of 12.3%. The wind tunnel model has a chord of $C = 0.23$ m and a blunt trailing edge measuring $0.005C$. The airfoil was mounted wall-to-wall and the boundary layer was tripped on both sides at $x/C = 0.07$ from the leading edge for fully-turbulent behavior. The results showed that a periodic self-sustained shock-wave motion (buffet) was obtained for angle of attack values higher or equal to 3.5°. A detailed experimental study, for this angle of attack, is reported in Jacquin et al. (2009). The main flow features concerning buffet were essentially two dimensional, and the buffet frequency was found 69–70 Hz. The shock-wave motion was coupled with an intermittent separation of the boundary layer. In the present study, this flow configuration is considered in two dimensions at an incidence of 3.5° and a free-stream Mach number of 0.73, in order to analyse the buffet onset and the interaction with the near-wake instability.

2.2. Numerical method

The simulations of the OAT15A configuration have been carried out with the Navier–Stokes Multi-Block (NSMB) solver. The NSMB solver is the fruit of a European consortium that included Airbus from the beginning of '90s, as well as main European aeronautics research Institutes, as KTH, EPFL, IMFT, ICUBE, CERFACS, Univ. of Karlsruhe, ETH-Ecole Polytechnique de Zurich, among other. This consortium is coordinated by CFS Engineering in Lausanne, Switzerland. NSMB is a structured code that includes a variety of efficient high-order numerical schemes and of turbulence modelling closures in the context of LES, URANS and of hybrid turbulence modelling. A first reference of the code description can be found in Vos et al. (1998) concerning the versions of this code in the decade of '90s. Since then, NSMB highly evolved up to now and includes an ensemble of the most efficient CFD methods, as well as adapted fluid–structure coupling for moving and deformable structures. These developments can be found in Hoarau (2002) regarding URANS modelling for strongly detached flows, Martinat et al. (2008), in the area of moving body configurations, Barbut et al. (2010) and Grossi et al. (2014) allowing for Detached Eddy Simulation with the NSMB code.

NSMB solves the compressible Navier–Stokes equations using a finite-volume formulation on multi-block structured grids.

In 3D cartesian coordinates (x, y, z), the unsteady compressible Navier–Stokes equations can be expressed in conservative form as

$$\frac{\partial}{\partial t}(\mathbf{W})+\frac{\partial}{\partial x}(\mathbf{f}-\mathbf{f}_v)+\frac{\partial}{\partial y}(\mathbf{g}-\mathbf{g}_v)+\frac{\partial}{\partial z}(\mathbf{h}-\mathbf{h}_v)=0, \tag{1}$$

where t denotes the time. The state vector W and the inviscid fluxes f, g and h are given in the following for the laminar model:

$$\mathbf{W}=\begin{pmatrix}\rho\\ \rho U\\ \rho V\\ \rho W\\ \rho E\end{pmatrix},\quad \mathbf{f}=\begin{pmatrix}\rho U\\ \rho U^2+p\\ \rho UV\\ \rho UW\\ U(\rho E+p)\end{pmatrix},\quad \mathbf{g}=\begin{pmatrix}\rho V\\ \rho VU\\ \rho V^2+p\\ \rho VW\\ V(\rho E+p)\end{pmatrix},\quad \mathbf{h}=\begin{pmatrix}\rho W\\ \rho WU\\ \rho WV\\ \rho W^2+p\\ W(\rho E+p)\end{pmatrix}. \tag{2}$$

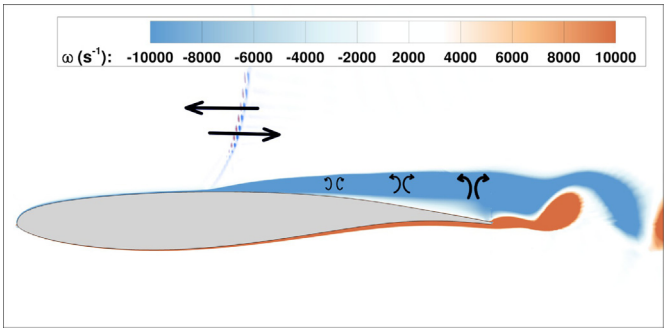

Fig. 1. Schematic diagram of shock, shear-layer and wake dynamics, including SWBLI, showing how the shear layer of the interface remains thin as a result of eddy-blocking mechanism.

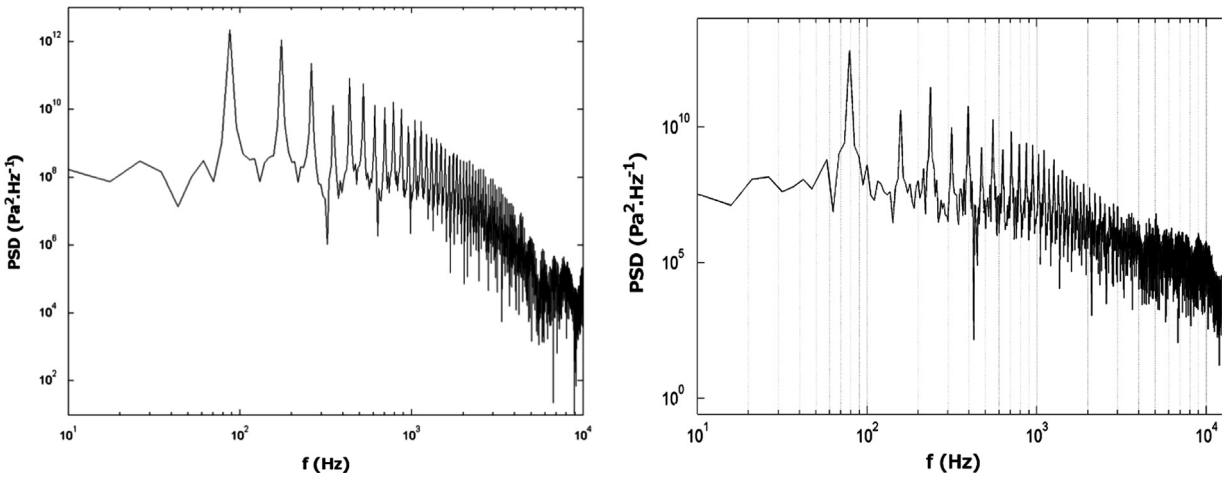

Fig. 2. Comparison of spectra of pressure signal for 2 different time steps; left: $\Delta t = 10^{-6}$ s; right: $\Delta t = 0.5 \times 10^{-6}$ s.

Here ρ is the density, U, V and W are the cartesian instantaneous velocity components, p is the pressure and E is the total energy. The viscous fluxes are defined as

$$\mathbf{f}_v = \begin{pmatrix} 0 \\ \tau_{xx} \\ \tau_{xy} \\ \tau_{xz} \\ (\tau\mathbf{U})_x - q_x \end{pmatrix}, \quad \mathbf{g}_v = \begin{pmatrix} 0 \\ \tau_{yx} \\ \tau_{yy} \\ \tau_{yz} \\ (\tau\mathbf{U})_y - q_y \end{pmatrix}, \quad \mathbf{h}_v = \begin{pmatrix} 0 \\ \tau_{zx} \\ \tau_{zy} \\ \tau_{zz} \\ (\tau\mathbf{U})_z - q_z \end{pmatrix}, \tag{3}$$

where τ_{ij} are the components of the stress tensor, q_i the heat flux (Fourier's law) and the work due to the viscous dissipation is expressed as $(\tau\mathbf{U})_i = \tau_{ix}U + \tau_{iy}V + \tau_{iz}W$.

The third-order of accuracy Roe upwind scheme (Roe, 1981) associated with the MUSCL van Leer flux limiter scheme (van Leer, 1979) is used to discretize the convective fluxes. Implicit time integration using the dual time stepping technique with 3 Gauss–Seidel iterations has been performed. A physical time step of 0.5 μs has been adopted ($\approx 5 \times 10^{-4} C/U_\infty$) after detailed tests carried out in Grossi (2010).

A study of the time step has been carried out with the grid used in this study. The Power Spectral Density (*PSD*) of the pressure signal on the airfoil at the location $x/C = 0.45$ for two time steps are shown in Fig. 2. The PSD spectrum on the left has been obtained from a calculation with a time step $\Delta t = 10^{-6}$ s, while the spectrum on the right comes from a calculation with a time step twice smaller and used in this study. A very similar distribution of the PSD can be observed in terms of frequency as well as of the energy level. A typical number of 30 inner iterations was necessary for the convergence in each time step. The convergence criterion at the inner step n is defined by the ratio between the L_2-norm of the density equation residual at the inner step n and the one at the initial inner step. The methodology adopted in the simulations is the same as in Grossi et al. (2014).

The grid has a C–H topology. Two different grids had been compared in previous studies (Grossi, 2014). The first is of size 110 000 cells approximately, used by Deck (2005) and provided within the partnership in the ATAAC (Advanced Turbulence Simulations for Aerodynamic Application Challengers) European program No. 233710 and a second, finer grid built in our research group, having 130,000 cells and a domain size of 80 chords. A comparison of these two grids is provided in Fig. 3. The mean value of the pressure coefficient (Fig. 3 left) and the RMS pressure distribution over the airfoil (Fig. 3 right) are very similar for the two grids. The buffet frequency is practically unchanged. The second grid has been used for the present

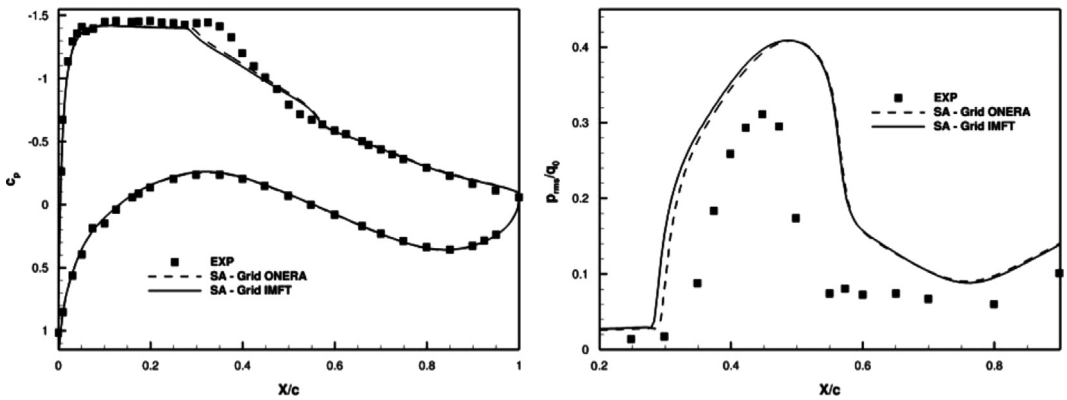

Fig. 3. Grid comparison concerning the mean wall-pressure coefficient (left) and the normalized *RMS* of the pressure fluctuations (right); experiment by Jacquin et al. (2009).

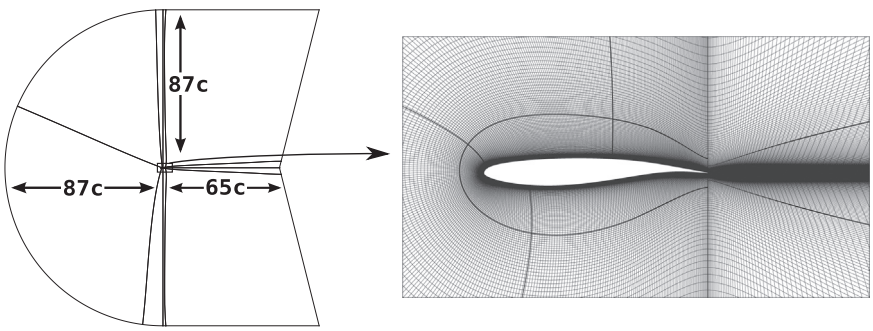

Fig. 4. Multiblock domain.

study. The y^+ coordinate regarding the turbulence modelling near the wall is smaller than 0.5 in the whole domain. Fig. 4 shows the grid and the computational domain.

2.2.1. Boundary conditions

On the solid wall, impermeability and no-slip conditions are employed. The far-field conditions are characteristic variables with extrapolation in time, defined by means of the experimental upstream values, the total pressure ($P_0 = 10^5$ Pa) and total temperature ($T_0 = 300$ K), as well as the upstream Reynolds number of 3 million. The upstream turbulence intensity is set equal to the experimental value of Tu = 1%.

2.3. Turbulence modelling

Based on previous studies in our research group which examined the predictive ability of various turbulence models (Grossi et al., 2011, 2012a; Grossi, 2014), it was shown that the two-equation $k-\omega$-SST model (Menter, 1994) was not able to produce any unsteadiness at the present incidence value. The Spalart-Almaras model (SA; Spalart and Allmaras, 1994) in its standard version, and its Edwards and Chandra variant (SA-E; Edwards and Chandra, 1996) with compressibility correction of Secundov (SA-E+CC; Shur et al., 1995; Spalart, 2000), underpredicted the amplitudes of the shock motion, even by tripping the flow at $x/C = 0.07$ like in the experiment (*trip*), which does not have a significant effect on the flow. The strain adaptive formulation of the Spalart–Allmaras model (SALSA; Rung et al., 2003) gave good amplitudes but no secondary oscillations. The $k-\varepsilon$-OES model (Braza et al., 2006; Bourguet et al., 2008) involving in the present study an eddy-diffusion coefficient $C_\mu = 0.03$, was able to produce the shock unsteadiness with a frequency close to the experimental one. Moreover,

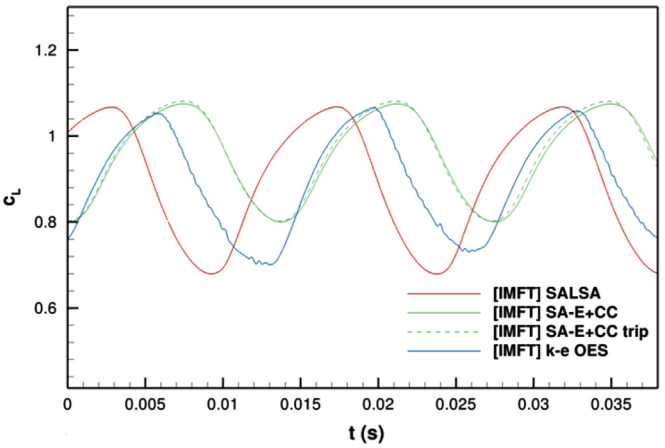

Fig. 5. Comparison of the time-dependent evolution of the lift coefficient between the strain adaptive formulation of the Spalart–Allmaras model (SALSA), the Edwards and Chandra variant of the Spalart–Allmaras model using compressibility corrections (SA-E+CC) without and with tripping at $x/C = 0.07$ (trip) and the $k-\varepsilon$-OES modelling.

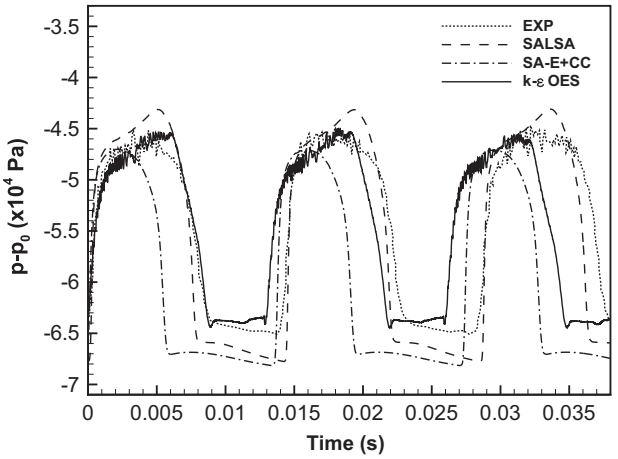

Fig. 6. Comparison of the time-dependent evolution of the surface pressure at $x/C = 0.45$ between three turbulence models as in Fig. 5; experiment by Jacquin et al. (2009).

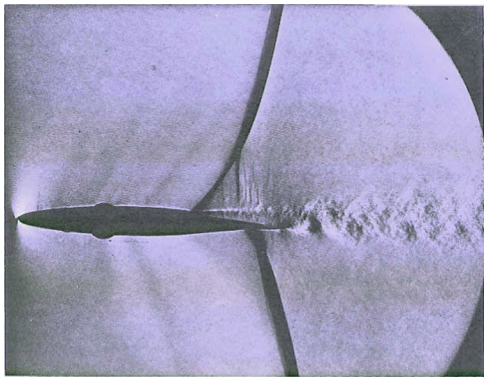

Fig. 7. Schlieren photograph of the eddying wake following a shock-induced flow separation (Courtesy of National Physical Laboratory, England; study by Duncan et al. (1932); photo by D.W. Holder.)

the formation of secondary oscillations within the buffet cycles, mainly due to intermittent von Kármán vortex shedding, has been captured. These results can be observed in Fig. 5 for the evolution of the lift coefficient and in Fig. 6 for the evolution of the pressure versus time at $x/C = 0.45$. The latter is compared with the experimental results from Jacquin et al. (2009) where the secondary oscillations are visible both in experiment and in the simulation with the $k-\varepsilon$-OES model.

3. Results

3.1. Buffet phenomenon and trailing-edge instabilities

According to the OES method, the resolved turbulence corresponds to an ensemble-averaged flow evolution, representing the organised, coherent part of the flow. A first overview of the buffet phenomenon and of the shear-layer and trailing-edge instabilities is represented in Fig. 8, by means of the velocity divergence field ($\nabla \cdot \mathbf{U} = \partial_x U + \partial_y V + \partial_z W$), which highlights compressibility effects around the airfoil and illustrates density gradients similar to the Schlieren visualizations. A qualitative similarity of the physical phenomena (shock waves, shock foot, wake) observed in the Schlieren visualization, for the experiment, by D.W. Holder (Fung, 2002; Fig. 7), and the field of divergence of velocity, for the CFD, is provided by the figures.

In the present study, the dimensionless time is $t^* = tU_\infty/C$. Furthermore, $t^* = 0$ was set to the maximum lift phase, with the shock wave at its most downstream position, as illustrated in Fig. 8(a). At that moment, in addition to the separation bubble at the foot of the shock, rear separation is also developed. These two regions grow simultaneously and fuse into a large separation area extending from the foot of the shock to the trailing edge. This scenario coincides with the well developed shock-wave motion towards the upstream direction, represented in Fig. 8(b). This figure shows the presence of a von Kármán instability, which quickly gives rise to alternate vortex shedding. In addition, Kutta-type waves are generated at the trailing edge of the airfoil and move upstream, at both sides of the airfoil. Upside, waves are refracted by the shock wave (Fig. 8(e)). As the shock moves towards the leading edge, the thickness of the separated region increases progressively, causing a dramatic decrease of the lift coefficient. As the shock wave comes towards its most upstream positions, the boundary layers becomes more and more detached. At the most upstream position (Fig. 8(f)), the reattachment process starts and reaches full reattachment while the shock is moving downstream (Fig. 8(g)), until $x/C = 0.60$ approximately (Fig. 8(h)). The alternate vortex shedding practically disappears, and the trailing-edge waves generation is temporarily attenuated, until the shear layer thickens again for a new cycle of buffeting.

The transonic flow around the symmetric NACA0012 airfoil (Bouhadji and Braza, 2003b), where a shock wave is observed on both upper and lower sides of the body, is cited in the introduction in order to comment the interaction between the buffet and the von Kármán modes. In the buffet regime ($M = 0.80$), the boundary layers downstream of the shock waves are alternately separated, inducing a thicker effective obstacle between the two separated shear layers that generates significant vorticity gradients in the trailing-edge region and hence creates the von Kármán mode. In the case of the supercritical OAT15A airfoil, at a slight angle of attack (3.5–3.9°), only one supersonic region exists at the upper side. In the buffet regime, the sequence of detachment and attachment still exists but only for the suction side. While the boundary layer is attached, the effective obstacle including the viscous region is thin enough to attenuate the vortex shedding which is only significant when the boundary layer is separated. It can be noted therefore that the shock wave, which thickens the boundary layer and the separated shear layers, creates favorable conditions for the von Kármán mode development, but this can happen even without buffet. In Bouhadji and Braza (2003a), where the successive stages of the von Kármán instability are analysed within a large Mach number interval including no-buffet and buffet regimes, the vortex shedding is developed according to the amplification of the von Kármán instability in the wake, as a result of the adverse pressure gradient due to the shape of the body, even without buffet appearance. Furthermore, at high Reynolds numbers ($1.4 \times 10^6 \leq \mathrm{Re} \leq 50 \times 10^6$), the von Kármán mode amplifies under similar conditions past a hydrofoil (incompressible flow; Bourgoyne et al., 2005). However,

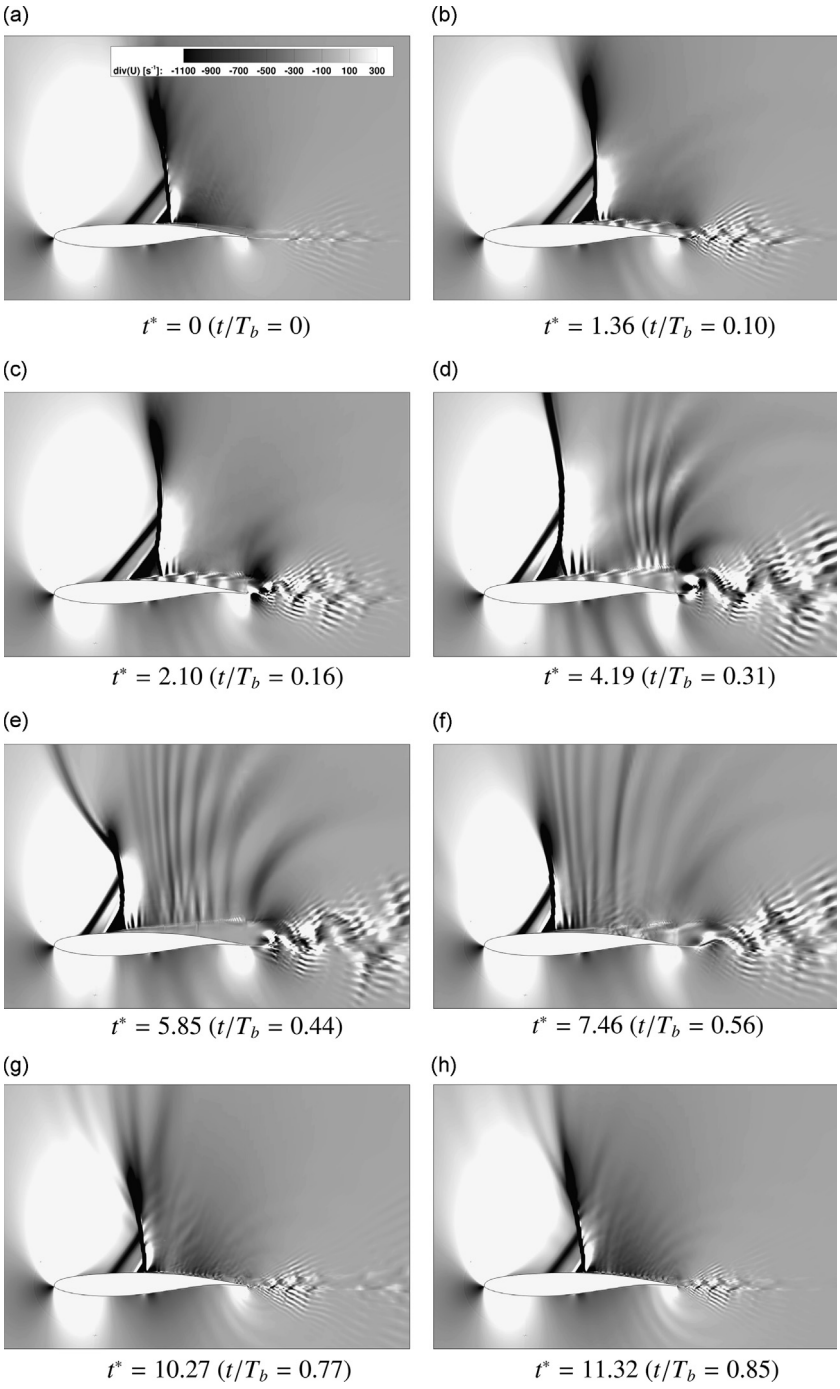

Fig. 8. Instantaneous fields of velocity divergence (T_b is the buffet period).

the buffet motion in the OAT15A test case thickens the boundary layer and hence favorizes the von Kármán mode appearance. The buffet also produces intermittently a thinning of the boundary layer when the shock moves downstream and leads to the intermittent disappearance of the von Kármán mode. Therefore, it can be mentioned that the buffet does not cause directly the von Kármán mode but it helps its appearance and disappearance.

3.2. Dynamic interaction between large-scale low-frequency shock motion and smaller-scale higher-frequency vortices

The buffeting process is analysed in more detail in terms of signal processing. Pressure signals containing 21 buffet periods and approximately 271 000 samples, have been recorded at the airfoil surface, as in the experiment of Jacquin et al.

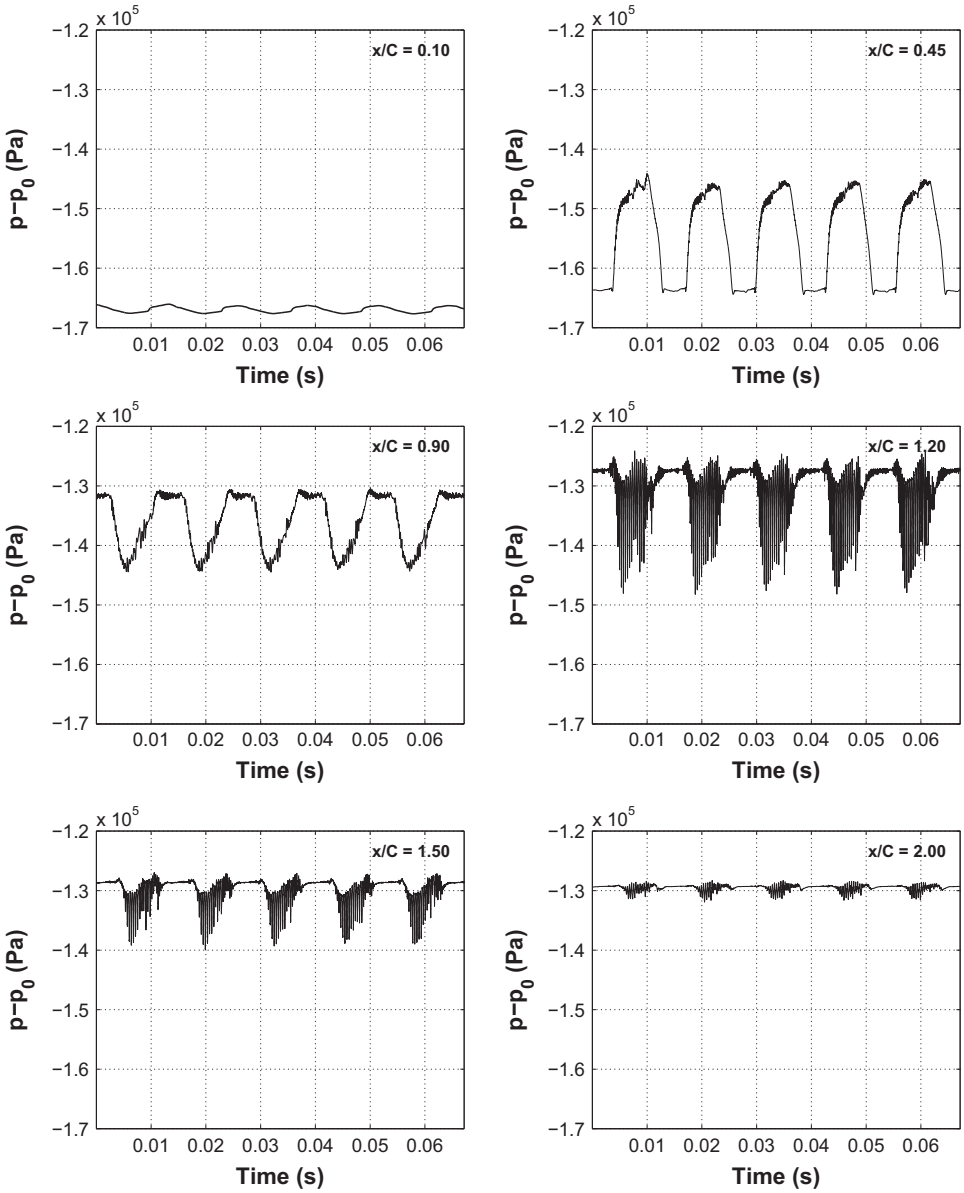

Fig. 9. Pressure fluctuations at the upper surface of the airfoil and in the wake.

(2009). In the present study, probe positions have been added in the wake, up to one chord downstream of the trailing edge. The sampling rate is 10^{-6} s. The signals are plotted in Fig. 9 for 5 buffet periods, at 6 positions from $x/C = 0.10$ to $x/C = 2.00$, and along $y/C = 0.03$ in the wake.

Upstream of the SWBLI, large-scale periodic oscillations corresponding to the buffet instability are obtained. At farther downstream positions, this mode is amplified, and secondary oscillations at a higher frequency appear. These oscillations, mainly generated near the trailing edge of the airfoil, reach a maximum amplitude in the near-wake at $x/C = 1.20$, and can be also observed in the div(**U**) field (Fig. 8). A significant part of these oscillations corresponds to a von Kármán mode, as will be discussed in the next section (Figs. 11 and 12). This mode presents a frequency modulation, due to the interaction with the trailing-edge and ambient turbulence, as highlighted by spectral analysis.

3.2.1. Spectral analysis

The mentioned instabilities and their interactions are studied by a spectral analysis and a time–frequency study using wavelets and auto-regressive (AR) modelling, allowing for frequency variation versus time. The spectra of the pressure fluctuations signals at four positions from $x/C = 0.10$ to $x/C = 1.20$ are presented in Fig. 10. The power spectral density is calculated by the Welch's overlapped segment averaging estimator in order to reduce the variance of the periodogram

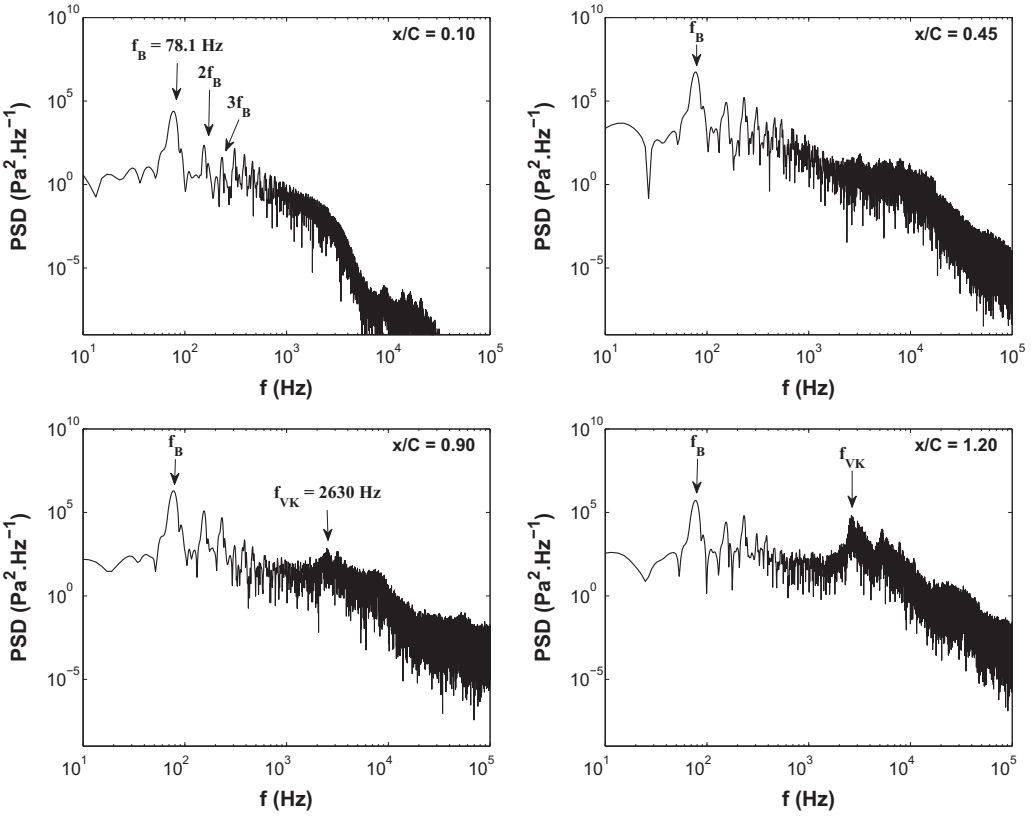

Fig. 10. PSD of the wall-pressure fluctuations at locations $x/C = 0.10$, 0.45 and 0.90 on the airfoil surface and at point $x/C = 1.20$, $y/C = 0.03$ in the wake.

(Welch, 1967). An overlapping of 80 % is applied on segments of size 60 % of the total length of the signal. Each segment is filtered by a Hanning window, and zero padding is used such that the number of samples on which the PSD is calculated equals to 2^{19}.

All the spectra show the appearance of the buffet frequency, at $f_B = 78.1$ Hz (St $= fC/U_\infty = 0.075$), and its harmonics. In the experiment, this frequency was equal to 69 Hz (St $= 0.066$). At the most upstream position ($x/C = 0.10$), the spectrum does not display any predominant frequency beyond 4000 Hz. Farther downstream ($x/C = 0.45$), the spectrum displays a more significant spectral amplitude and more rich turbulence content in the area beyond 4000 Hz. This occurs because of the influence of the separated region downstream of the SWBLI. At this position, the spectrum can be compared with the experimental results (Jacquin et al., 2009, Fig. 10). In the range of frequencies available on the spectrum from the experiment, both spectra are similar in terms of the buffet frequency and its harmonics, although the shape of the peaks are different, which is due to the number of buffet periods (order of 20) in the numerical study which is less than in the experimental study. At this farther downstream position, the main mode is amplified and secondary oscillations at a higher frequency appear. This phenomenon becomes more pronounced for positions near the trailing edge ($x/C = 0.90$) and in the near-wake ($x/C = 1.20$; see Fig. 8). At $x/C = 0.90$, the power spectral density distribution can be compared with other URANS simulations (Brunet et al., 2003, Figs. 11 and 18). The comparison of the spectral peak amplitude and their frequency are close between the present study and the above reference. A frequency peak appears at around 2600 Hz (St $= 2.5$). This peak becomes more pronounced at $x/C = 1.20$.

We can show that this frequency corresponds to the von Kármán vortex shedding. Fig. 11 presents snapshots of the vorticity field taken at four equidistant time intervals in respect of the period 1/2600 s. These fields clearly show the alternating von Kármán vortex shedding and the periodicity of the vortex pattern from $t = 0.00962$ s to $t = 0.01$ s. In order to quantify the frequency of this vortex shedding, a tracking of the vorticity values versus time has been carried out at the locations 1 and 2 (see Fig. 11) during one buffet period. The vorticity signals and their spectra are presented in Fig. 12, where a bump is identified at 2600 Hz. This fact insures the identification of a von Kármán mode at the present frequency.

The peak localized at 2600 Hz in the spectra of the pressure signals is characterised by a spreading of frequencies (spectral 'bump'). This is mainly due to a strong interaction of the von Kármán mode with the trailing-edge unsteadiness (appearance of grey fringes related to Kutta waves in the div(**U**) plots, Fig. 8) and to the turbulent motion. This spectral region is studied in more details in the next section, by means of time–frequency analysis.

Moreover, the Kelvin–Helmholtz vortices shown in Fig. 8(c) in the detached shear layer downstream of the shock foot can be identified by tracking them during the time-interval of 0.24 μs. Their convection velocity has been assessed of order

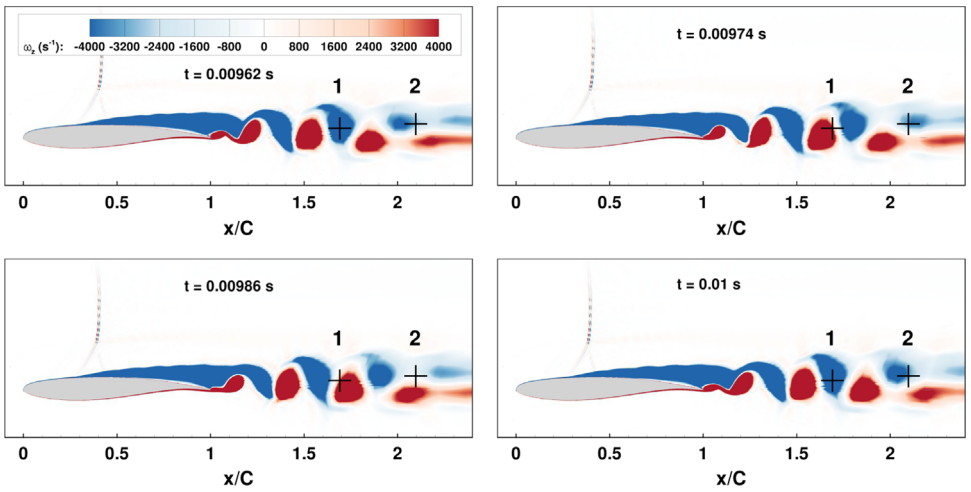

Fig. 11. Four instantaneous vorticity fields covering one period of trailing-edge vortex shedding and showing probing locations of the vorticity values used in next figure.

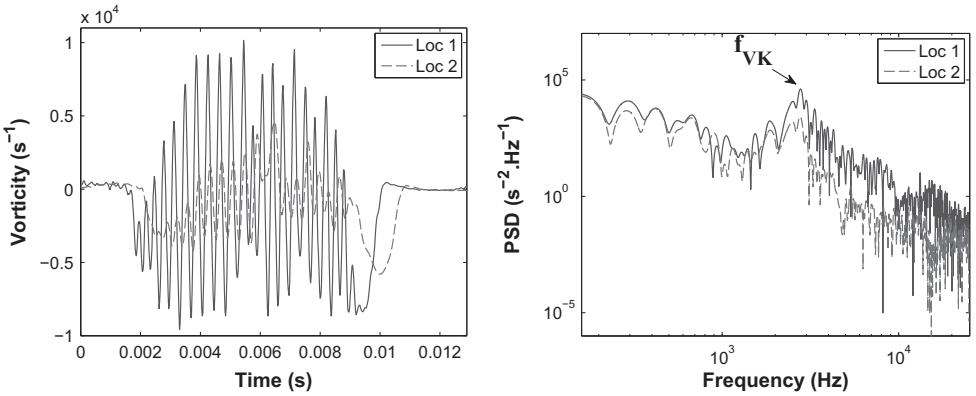

Fig. 12. Vorticity signals in the wake (left) and their power spectral density (right).

202 $\mathrm{m}\cdot\mathrm{s}^{-1}$, as well as their wavelength, λ, of order 1.9×10^{-2} m. From these parameters, their shedding frequency has been assessed of order 10^4 Hz (St $=9.5$) from the relation $U_{\mathrm{conv}}=\lambda\cdot f$. This is higher than the von Kármán frequency. By considering the energy spectrum at $x/C=1.20$ and $y/C=0.03$ with suitable window size and zero padding in order to better visualize the region of frequencies around 10^4 Hz (Fig. 13), a predominant frequency peak at 10^4 Hz can be identified, which corresponds to the Kelvin–Helmholtz shedding frequency.

As previously mentioned, the buffet frequency is found 78.1 Hz in the current study, while the vortex shedding frequency is about 2600 Hz when this phenomenon is well established. The ratio of these two frequencies is 33.29. The closest buffet harmonic regarding the von Kármán peak is $78.1\times33=2577$ Hz. This frequency slightly varies inside each buffet cycle, and from a cycle to another, which produces the bump observed in the spectra around 2600 Hz. This increases the uncertainty of this frequency value. As shown in the spectrum of Fig. 14, the higher buffet harmonics "merge" with the von Kármán bump onset and a synchronization may occur with von Kármán subharmonics. This interaction is difficult to analyse because the amplitudes of these higher harmonics and subharmonics are somehow "hidden" in the continuous part of the spectrum between the two events, the buffet and the von Kármán frequency peaks.

It is recalled that the present study aims at analysing the trailing-edge instabilities in association with the buffet mode. The fluctuations related to the von Kármán instability appear less explicitly in the spectra in Jacquin et al. (2009), Deck (2005), as well as in Thiery and Coustols (2005) and Brunet et al. (2003), because the main objective of these studies focused on the buffet phenomenon. Indeed, these studies measure the pressure fluctuations on the airfoil wall, with the most downstream position of the measurements located at $x/C=0.90$, where the level of the von Kármán fluctuations is still very small and the experimental spectrum cut-off is lower than the expected von Kármán frequency, captured by the present numerical study, which displays existence of a spectral bump region around a predominant frequency of order 2600 Hz (Fig. 10, see spectrum at $x/C=0.90$). As has been previously shown, this frequency corresponds to the alternating vortex shedding in respect of the von Kármán mode. In this figure, concerning a more downstream position in the wake, $x/C=1.20$, this spectral bump clearly appears.

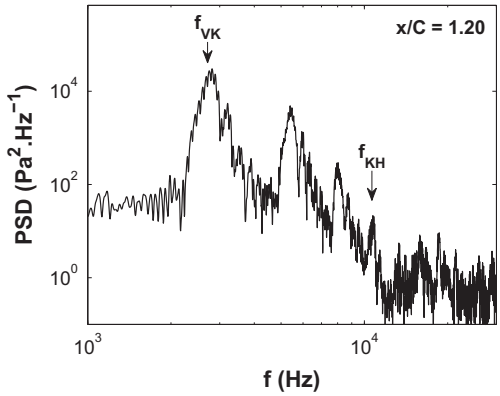

Fig. 13. PSD of pressure fluctuations at $x/C = 1.20$, $y/C = 0.03$. Detailed view of the range $10^3 - 3 \times 10^4$ Hz.

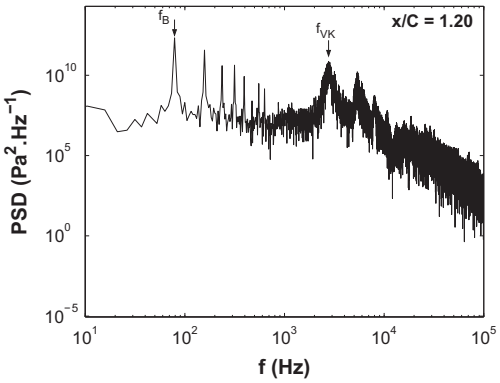

Fig. 14. PSD of pressure fluctuations at $x/C = 1.20$, $y/C = 0.03$.

In Fig. 20 of the experimental study by Jacquin et al. (2009), which displays four instants of the phase-averaged longitudinal velocity field, there is no proof of vortex shedding as identified in our study. This can be explained because a section of the wake is not visible due to the experimental setup, and also because the phase averaging, based on the buffet cycle, may have erased the marks of the vortex shedding, which has a frequency more than 30 times higher than the buffet one, and a phase which is not synchronized with the buffet. Figs. 15 and 16 of the present study show the instantaneous and the phase-averaged longitudinal velocity fields respectively, at four phases of the buffet cycle, similarly to the experimental results of Jacquin et al. (2009). These figures show the periodic motion of the accelerated region due to the buffet, as well as the boundary-layer detachment. In fact, the von Kármán vortices are visible in the instantaneous fields using a similar color scale as in the experimental results, but they are attenuated after phase-averaging over two buffet periods only (Fig. 16). Regarding Fig. 12 of Deck (2005) that displays the divergence of the velocity field, the color scale can be adapted in order to highlight the vortex shedding structures, as the divergence of velocity is much smaller within the vortices than in the area of the shock wave and Kutta waves. However, an alternating pattern can be distinguished in this figure too. If the above mentioned studies had been interested in the near-wake region and under the condition that the experimental and numerical grids be sufficiently fine in the wake, they would have been able to capture the von Kármán instability too. However, this was not an objective of the mentioned studies. An evidence of the existence of the von Kármán mode in these experiments can be seen in the appearance of secondary fluctuations observed in the experimental measurements of the time evolution of the pressure at $x/C = 0.45$ (Jacquin et al., 2009, Fig. 8). If the spectrum of Fig. 10 in Jacquin et al. (2009) would display a frequency range beyond 10^3 Hz, the von Kármán mode would also appear. This mode is characterised by a spectral bump, showing that it is subjected to the influence of other, more chaotic events in the time-space evolution. Moreover, small vortices in the trailing-edge region have been measured by Brunet et al. (2003), in URANS simulations of the OAT15A test case, but at a higher angle of attack ($\alpha = 5^\circ$). Their signature seems to appear as a spectral bump in Fig. 11 of this reference. These vortices can also be observed in the Schlieren visualization in Fig. 7. Von Kármán vortices were also reported in several experiments on subsonic compressible flows around airfoils (Alshabu and Olivier, 2008; Fung, 2002) as well as in the direct simulation of transonic buffet at lower Reynolds numbers by Bouhadji and Braza (2003b) and Bourdet et al. (2003).

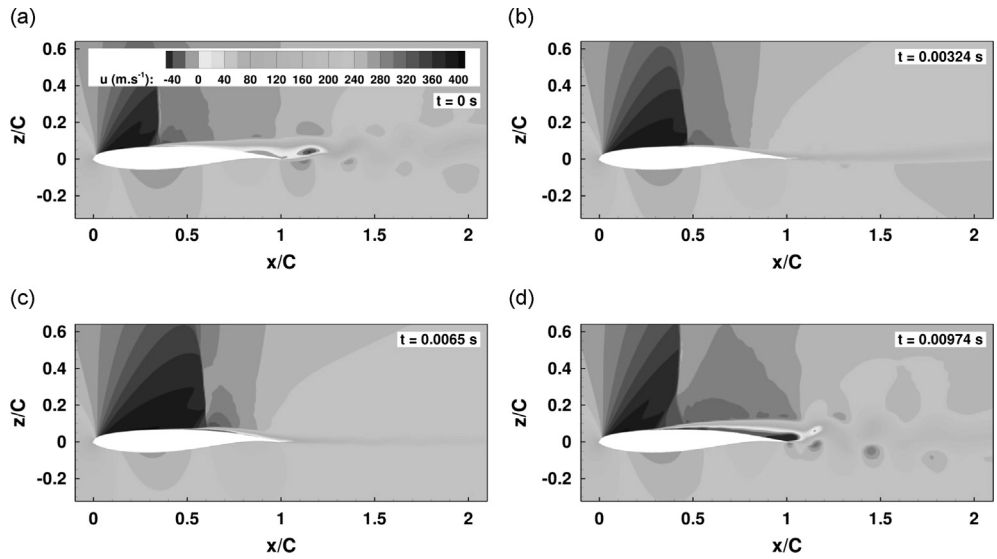

Fig. 15. Instantaneous longitudinal velocity at 4 phases of a buffet cycle: (a) shock upstream; (b) shock moving downstream; (c) most upstream position of the shock; (d) shock travelling upstream.

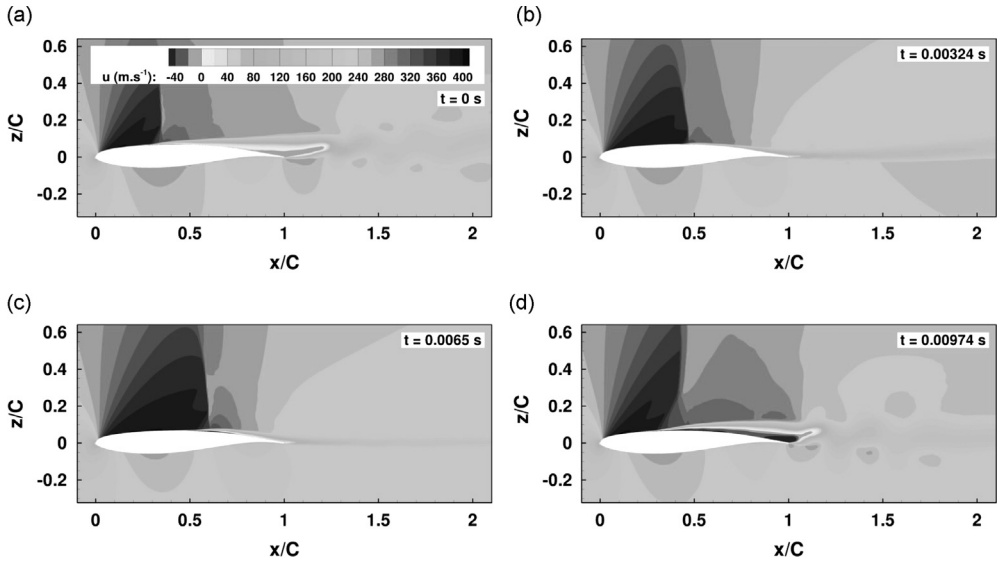

Fig. 16. Phase-averaged longitudinal velocity at 4 phases of a buffet cycle: (a) shock upstream; (b) shock moving downstream; (c) most upstream position of the shock; (d) shock travelling upstream.

3.2.2. Time–frequency analysis

The pressure signal in the wake at $x/C = 1.20$, a position where the amplitude of the secondary instabilities is maximum, corresponding to the bursts formed in the pressure evolution and to the spectral "bumps" (Figs. 9 and 10 respectively), are governed by the von Kármán mode and instabilities mainly coming from the trailing edge and the shear layers. This signal is filtered by a high-pass filter with a cutoff frequency of 1577 Hz, by means of Fast Fourier Transform (*FFT*). The filtered pressure signal, shown in Figs. 17 and 18, designated as P_f (f standing for filtered), is reconstructed by the inverse *FFT*. The physical phenomena whose frequency is higher than 1577 Hz are conserved. The remaining signal shows now more clearly the buffet effect on the higher-frequency phenomena within each buffet cycle (burst). Each burst contains an order of 15 counter-rotating vortex-shedding pairs, as well as time intervals where the vortex shedding is considerably attenuated. The instability evolution within the burst is studied by means of time–frequency analysis, carried out by a continuous wavelet transform, and segmentation of the filtered signal. The complex Morlet wavelet (Grossmann and Morlet, 1984) is used to

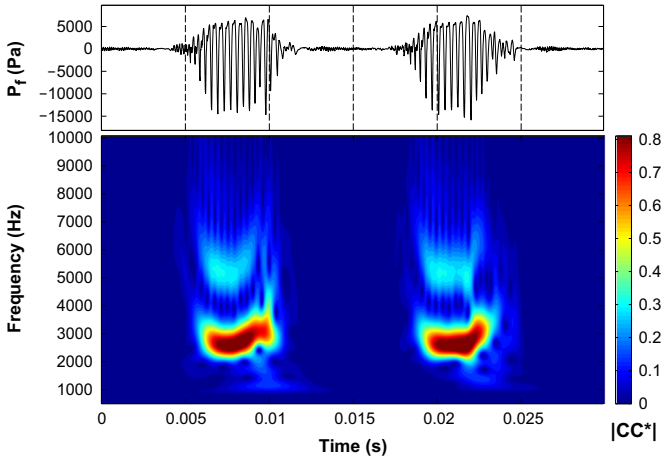

Fig. 17. Normalized absolute value of complex continuous wavelet transform coefficients.

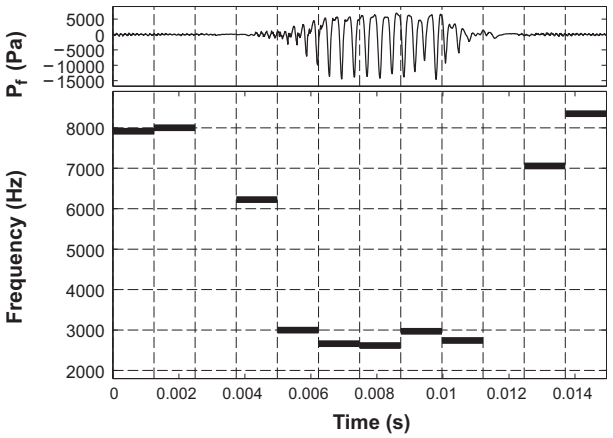

Fig. 18. Time–frequency analysis of the filtered pressure signal at $x/C = 1.20$, $y/C = 0.03$, using autoregressive modelling.

analyse two buffet periods:

$$\psi(t) = \frac{1}{\sqrt{4\pi}} e^{2i\pi f_0 t} e^{-t^2/2}, \tag{4}$$

where f_0 is the central frequency of the wavelet.

The wavelet transform coefficients are defined as

$$C(a,b) = \frac{1}{\sqrt{a}} \int_{-\infty}^{\infty} x(t)\ \psi^*\left(\frac{t-b}{a}\right) dt \tag{5}$$

where a and b are the scaling (in frequency) and the location (in time) parameters of the wavelet respectively, $x(t)$ the signal and ψ^* is the complex conjugate of the wavelet. The absolute value of these wavelet transform coefficients, $|C\ C^*|$, is plotted in Fig. 17. The scalogram allows analysing in more details the evolution of the vortex shedding frequency versus time inside each buffet cycle. When the shock starts moving upstream (Fig. 8(b)), the vortices are shed at a frequency of 4000 Hz with low amplitudes (see beginning of the burst Fig. 17). Afterwards, this frequency diminishes to reach 2600 Hz, which is the von Kármán frequency observed in the spectra. The vortex shedding is then well established within the burst and is maintained until the shock reaches its most upstream position (see evolution of the shock motion, Fig. 8(c)–(f)). Next, the generated vortices become smaller (Fig. 8(g)) and the shedding frequency increases to reach again the initial value of 4000 Hz, before this phenomenon be significantly attenuated and vanish while the shock moves downstream and the boundary layer becomes attached (Fig. 8(h)–(a)). This frequency modulation, associated with the location and size of the alternating vortices versus time, is linked to the spectral bump appearance around the von Kármán mode (Fig. 10). The repetitiveness of this modulation is clearly observed in the scalogram. The first harmonic is also present with the same modulation. Fig. 18 presents the frequency variation of the pressure coefficient versus time during one buffet period, by using the Yule–Walker autoregressive (AR) model. This kind of model conceptually ensures a high accuracy in the estimation of the frequency values versus time (Braza et al., 2001). The Yule–Walker equations, obtained by fitting the autoregressive

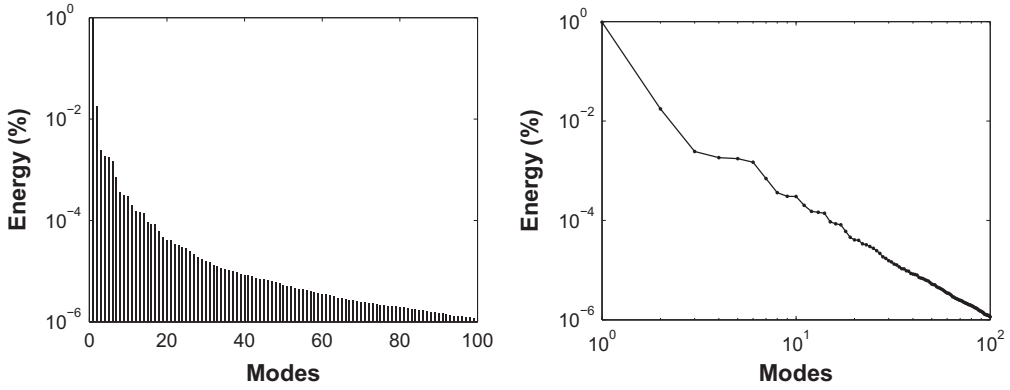

Fig. 19. Energy distribution of the POD modes (semi-log and log–log diagrams).

linear prediction filter model to the signal, by minimizing the forward prediction error in the least squares sense, are solved by the Levinson–Durbin recursion (Durbin, 1960). This method is applied with an AR order of 210 on a signal including a one burst cycle. 14 952 samples are used and the signal is segmented in windows of 1153 points. The fundamental frequency of each segment is obtained by calculating the PSD of the modelled signal, using zero-padding giving 2^{21} samples. The result of this method shows the same frequency modulation during the vortex shedding occurrence, as in case of the continuous wavelet transform.

In the next section, a POD analysis is presented which includes additional aspects of the interaction among the buffet, the von Kármán and the smaller-scale higher-frequency vortices, especially those of the shear layers.

3.2.3. *Proper orthogonal decomposition*

Based on the time-space solution from the previously mentioned simulations, a proper orthogonal decomposition (POD) has been carried out on the ensemble-averaged flow-fields, based on the separable POD method in respect of space and time (Sirovich, 1990; Aubry et al., 1991), as presented in the following relations. The POD modes are evaluated from a series of successive snapshots, which include in the present case 10 buffet periods. 646 snapshots, recorded by using a sampling rate of 10^{-5} s, are used per buffet period. As the first POD mode corresponds to the time-averaged solution contained in the data, the POD modes from order 2 correspond to the fluctuating part of the velocity fields:

$$\mathbf{U}(\mathbf{x},t)=\overline{\mathbf{U}}(\mathbf{x})+\mathbf{u}(\mathbf{x},t)=\overline{\mathbf{U}}(\mathbf{x})+\sum_{n=2}^{N_{\mathrm{POD}}}a_n(t)\boldsymbol{\phi}_n(\mathbf{x}), \tag{6}$$

where $\overline{\mathbf{U}}$ and $\mathbf{u}$ denote the mean and fluctuating parts of the velocity, respectively. The fluctuation mainly includes the effects of the buffet, von Kármán and shear-layer instabilities. This fluctuation includes the following contributions:

$$\mathbf{u}(\mathbf{x},t)=\tilde{\mathbf{u}}(\mathbf{x},t)+\check{\mathbf{u}}(\mathbf{x},t)+\hat{u}(\mathbf{x},t), \tag{7}$$

where $\tilde{\mathbf{u}}$ is the phase-averaging, $\check{\mathbf{u}}$ is the downscale contribution of the fluctuation, and $\hat{u}$ is the upscale one. Following a simple algebraic development for the decomposed phase-averaged Navier–Stokes equations, it can be shown that the new turbulent stresses contain a downscale part: $\langle\check{u}_i\check{u}_j\rangle$, and a cross term: $\hat{R_{ij}}=\langle\check{u}_j\hat{u}_i\rangle+\langle\hat{u}_j\check{u}_i\rangle+\langle\hat{u}_j\hat{u}_i\rangle$. As will be discussed in the next section, $\hat{R_{ij}}$ will be modelled by a stochastic forcing. At this stage, a major contribution is due to the downscale term.

The normalized shape-functions $\boldsymbol{\phi}_n$ are spatially orthogonal, while the temporal coefficients a_n are uncorrelated in time:

$$\left\langle\boldsymbol{\phi}_i\cdot\boldsymbol{\phi}_j\right\rangle=\delta_{ij}\quad\text{and}\quad\overline{a_i a_j}=\delta_{ij}\lambda_i. \tag{8}$$

The brackets and overbar indicate spatial integration and temporal averaging, respectively. λ_i is the eigenvalue of mode *i*. δ_{ij} is the Kronecker delta. The POD modes $\boldsymbol{\phi}_n$ are obtained as the eigen-modes of the two-point correlation matrix:

$$\overline{\overline{\mathbf{C}}}\boldsymbol{\phi}_n=\lambda_n\boldsymbol{\phi}_n\quad\text{with}\quad C_{ij}=\overline{\mathbf{u}(\mathbf{x}_i,t)\cdot\mathbf{u}(\mathbf{x}_j,t)}. \tag{9}$$

The eigenvalue λ_n represents the contribution of the corresponding POD mode to the total fluctuating energy:

$$\left\langle\overline{\mathbf{u}(\mathbf{x}_i,t)\cdot\mathbf{u}(\mathbf{x}_j,t)}\right\rangle=\sum_{n=1}^{N_{\mathrm{POD}}}\lambda_n. \tag{10}$$

Fig. 19 shows the energy of the POD modes as a function of the mode order. There is an energy decrease towards the higher modes. The decrease rate is slower than in DNS cases (El Akoury et al., 2008), because of the random turbulence effect, modelled by the solved transport equations. In the log–log energy diagram, a “plateau” followed by a slope change is observed. This feature represents the contribution of the organised motion and of the random turbulence effect, which

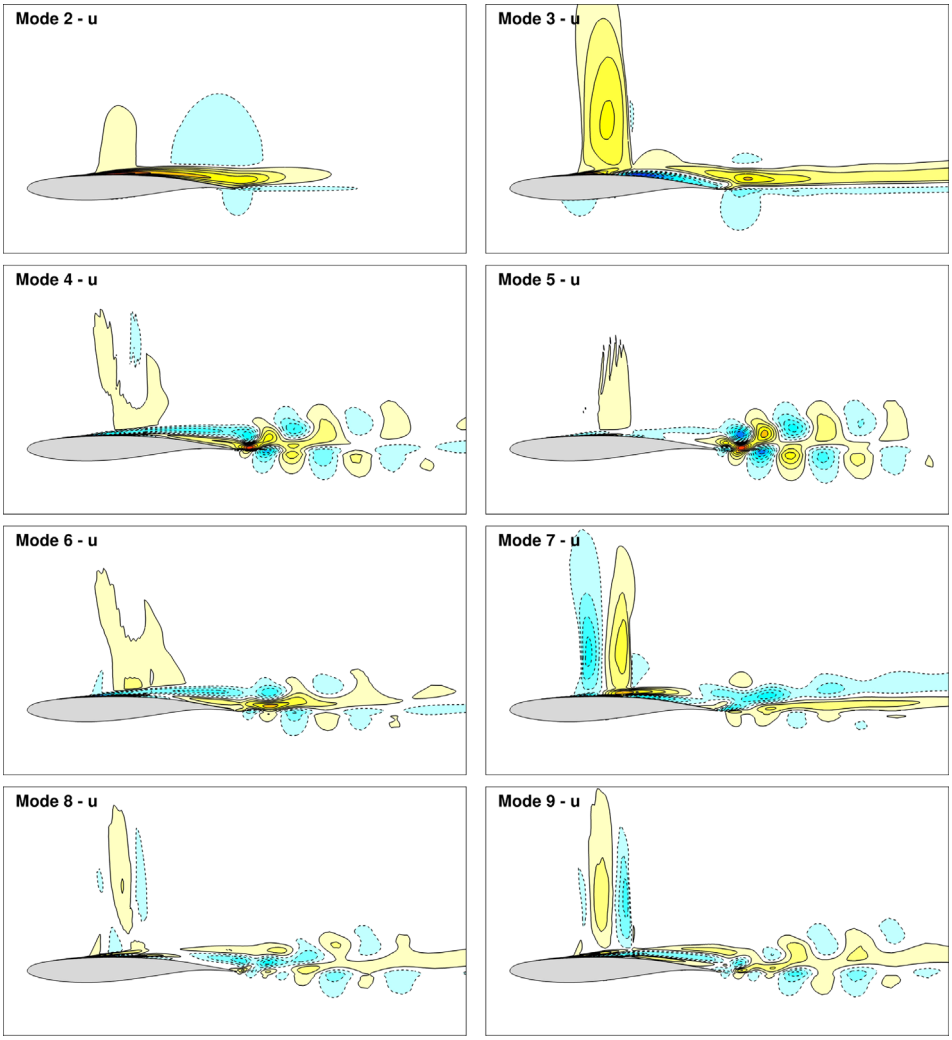

Fig. 20. First POD modes associated with the streamwise velocity.

becomes more pronounced, as the mode order increases. A similar behaviour was reported in experimental studies by Perrin et al. (2006).

The POD analysis allows extracting the most energetic modes (Fig. 20) which can reconstruct the main features of the interaction between the buffet and the downstream region as shown in the following. The modes 2 and 3 of the streamwise velocity U illustrate the buffet phenomenon and the boundary-layer intermittent detachment (Fig. 20).

Modes 4 and 5 clearly illustrate the von Kármán motion. A complex interaction among the buffet region (shock), the shear layer past the SWBLI and the von Kármán mode past the trailing edge is shown by means of the higher order modes. This interaction leads to creation of a more pronounced chaotic process (modes 6 and 7), because the frequencies of the mentioned instabilities are incommensurate. Furthermore, the von Kármán mode iso-contour levels affect also the shock-motion region (modes 4–9).

The temporal POD coefficients are shown in Fig. 21. They are in accordance with the spatial mode behaviour. As the order of the modes increases, a filling-up of the temporal coefficient signal by higher frequencies is noticed, showing the increasing complexity of the dynamic system, due to turbulence.

The energy spectra of the temporal POD coefficients for modes 2–9 are presented in Fig. 22. The first spectrum indicates the buffet frequency as a predominant one and confirms the fact that mode 2 is associated with this instability. The POD modes higher than 3 start progressively to be affected by the von Kármán instability, as shown also in the spatial distribution of these modes, Fig. 20. The amplitude of the von Kármán instability (Fig. 22) increases for modes 4 and 5, to reach a practically invariant level in the higher mode spectra. Simultaneously with this variation, the buffet instability amplitude decreases on the spectra and its harmonics slightly increase but the global level of the buffet instability amplitude remains lower than in case of the third POD mode. Therefore, in the mode ranges 4 and 5, the spectral amplitudes of the von Kármán and of the buffet become comparable.

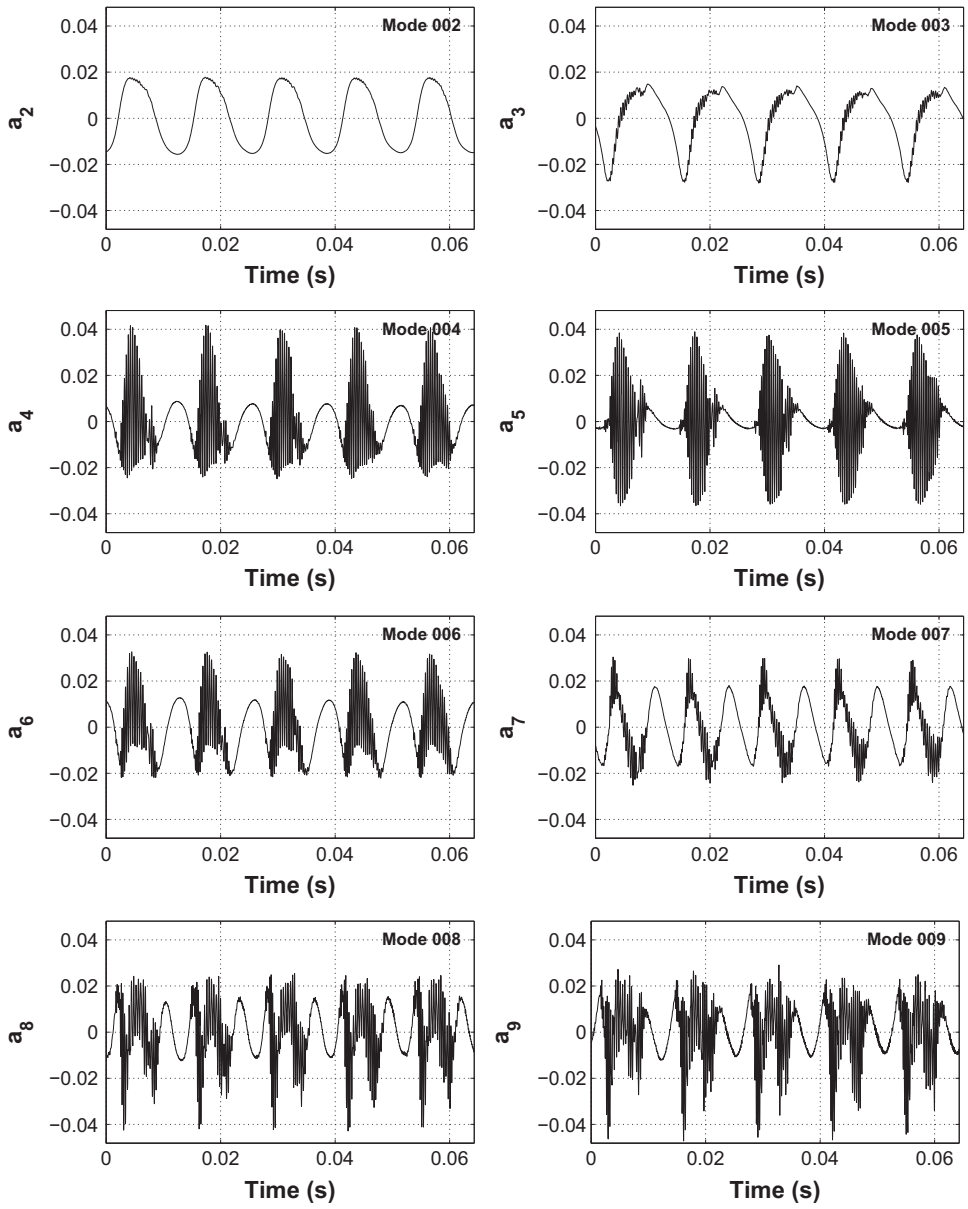

Fig. 21. Temporal coefficients a_n of the first POD modes.

From the dynamic system theory point of view, a non-linear interaction between two incommensurate instability modes that are rather close in terms of frequency produces linear combinations of these two modes in the energy spectrum (Newhouse et al., 1978; Guzmán and Amon, 1994). In the POD spectrum of mode 2 (Fig. 22), the interaction between the higher buffet harmonics and the von Kármán subharmonics is more visible, because these two sets are neighbours. We can detect for example a predominant frequency bump, f_{i1}, which can be expressed as $f_{VK}/2-5f_B$. Moreover, a second interaction can be extracted, $f_{i2}=f_{VK}/2-8f_B$. These interactions, as in the aforementioned papers, do not considerably change the frequency values of the instability modes (buffet and von Kármán). They rather change the amplitudes of these modes, which become comparable between the buffet mode and the von Kármán, as shown in Fig. 22 (spectra of POD modes 4 and 5, as well as spectra of POD modes 6 and 7). This illustrates a way the buffet mode is affected by the shedding mode and vice-versa.

The spectra of modes 12 and 13 are presented in Fig. 23. They show a broadening of the von Kármán area associated with the interaction between smaller-scale higher-frequency vortices (as for example the K–H around 10^4 Hz) and more chaotic turbulence effects. This fact persists for all the higher order modes. The corresponding spectra are plotted in Fig. 27 and they confirm this observation.

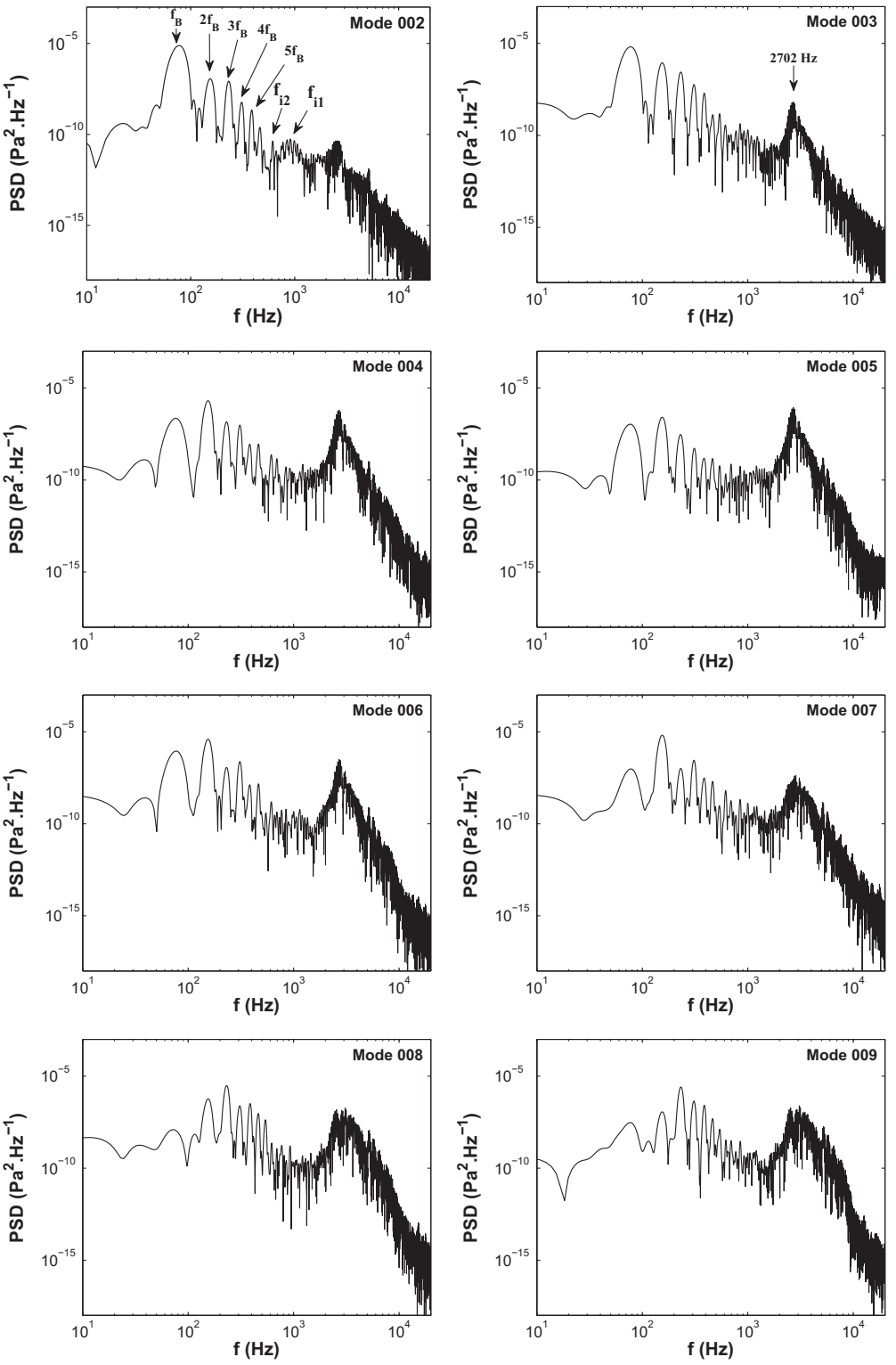

Fig. 22. PSD of POD mode temporal coefficients.

Based on the present discussion, the POD analysis illustrates in a complementary way the interaction between the buffet and the von Kármán modes as well as with the higher frequency structures, by means of the mode shape and the temporal coefficients amplitude modulations, as well as by the appearance of new frequency peaks in the spectra combining these instabilities.

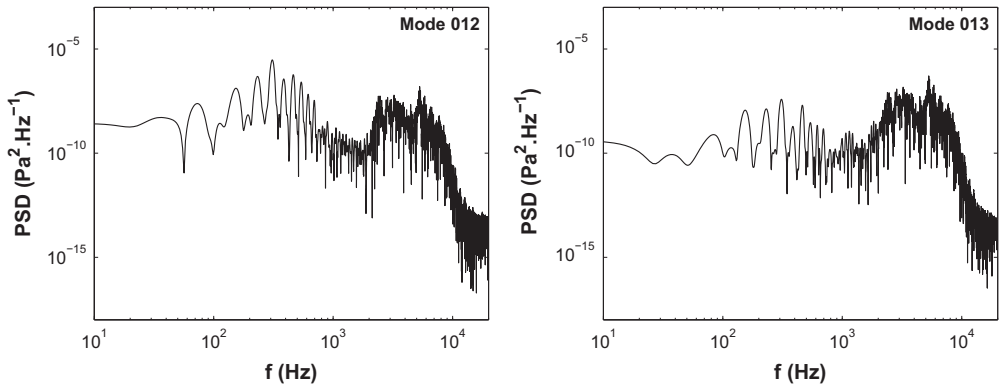

Fig. 23. PSD of temporal coefficient of POD modes 12 and 13.

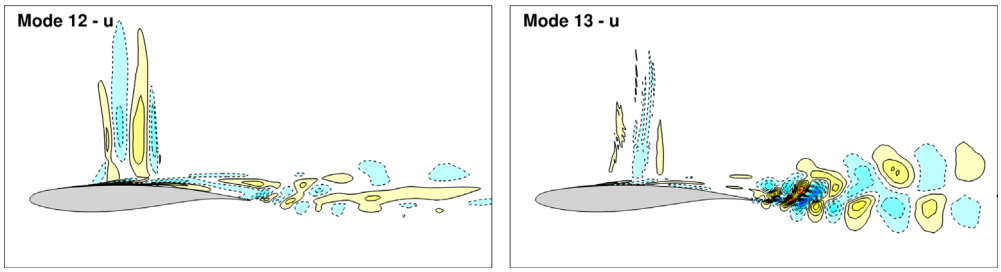

Fig. 24. POD modes 12 and 13 associated with the streamwise velocity.

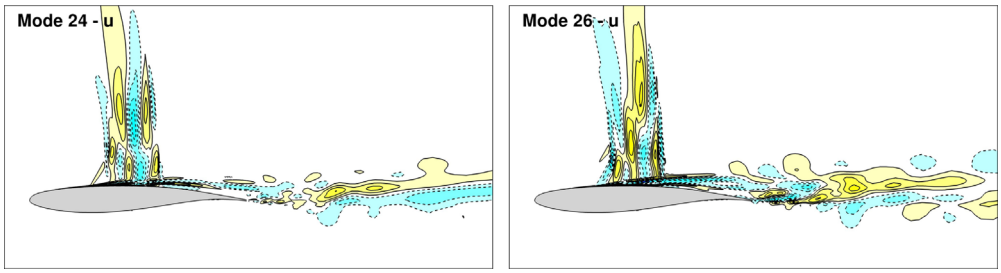

Fig. 25. Intermediate-range POD modes associated with the streamwise velocity.

Furthermore, the POD analysis illustrates the signature of the Kelvin–Helmholtz vortices (Figs. 24–26). In the 12th and 13th POD mode fields, the development of the lower shear-layer structure past the trailing edge can be observed. In the 24th and 26th mode fields, the impact of the upper shear-layer vortices can be seen. The higher POD modes (Fig. 26) influence all the high shearing rate regions, including also the shock area. Therefore, these figures show the filling of the shear layers by smaller-scale structures and illustrate their interactions with the shock-motion area. Indeed, the iso-contour levels of these smaller structures fill up the shock-motion region (Figs. 25 and 26).

4. Stochastic forcing by means of POD

The shear-layer interfaces between the turbulent and non-turbulent regions are now considered in association with those POD modes which particularly affect these areas as previously discussed. In order to maintain these interfaces thin and to limit the turbulent diffusion effect due to the direct cascade modelling assumptions, a small amount of kinetic energy is introduced as a "forcing" in the transport equations of the k and ε variables, acting as a "blocking effect" of the vorticity in the shear layer as in the schematic representation of Fig. 1, according to Westerweel et al. (2009). This small kinetic energy can be constructed from the "residual" high-order POD modes previously presented, by reconstructing fluctuating velocity components derived from the use of the last POD modes of very low energy. Therefore, an *inhomogeneous* stochastic forcing can be built and used as a source term in the transport equations regarding k (Eq. (11)) and ε (Eq. (12)). This term contains a small fluctuating velocity scale which acts within the shear layer and in the region below, without affecting the regions beyond the turbulent/non-turbulent interface. By dimensional analysis, this kind of source terms can take the form of Eq. (13), where the ambient value of the turbulent kinetic energy is $k_{\text{amb}} = k_{fs} U_\infty^2$, and $k_{fs} = 3/2\ \text{Tu}^2$, with Tu the upstream

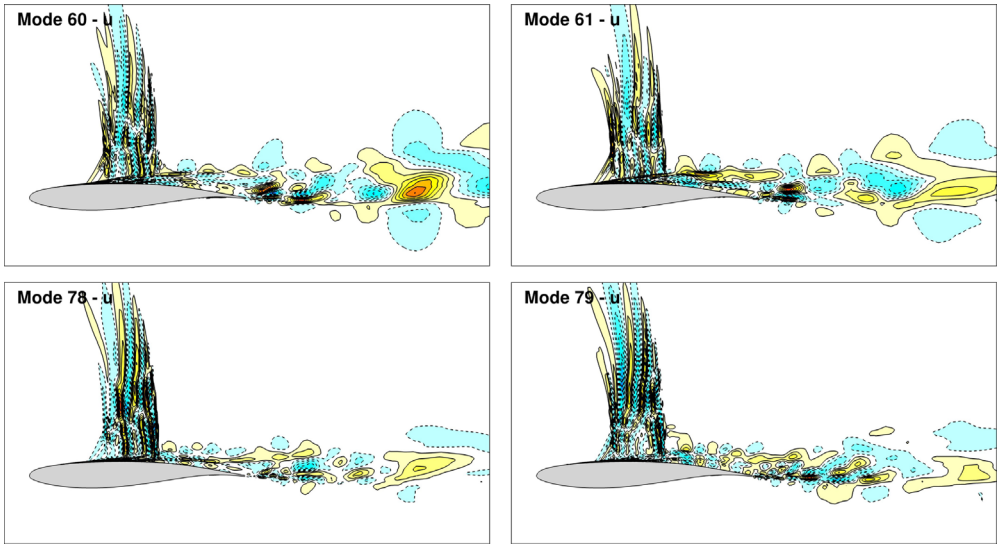

Fig. 26. Higher-range POD modes associated with the streamwise velocity.

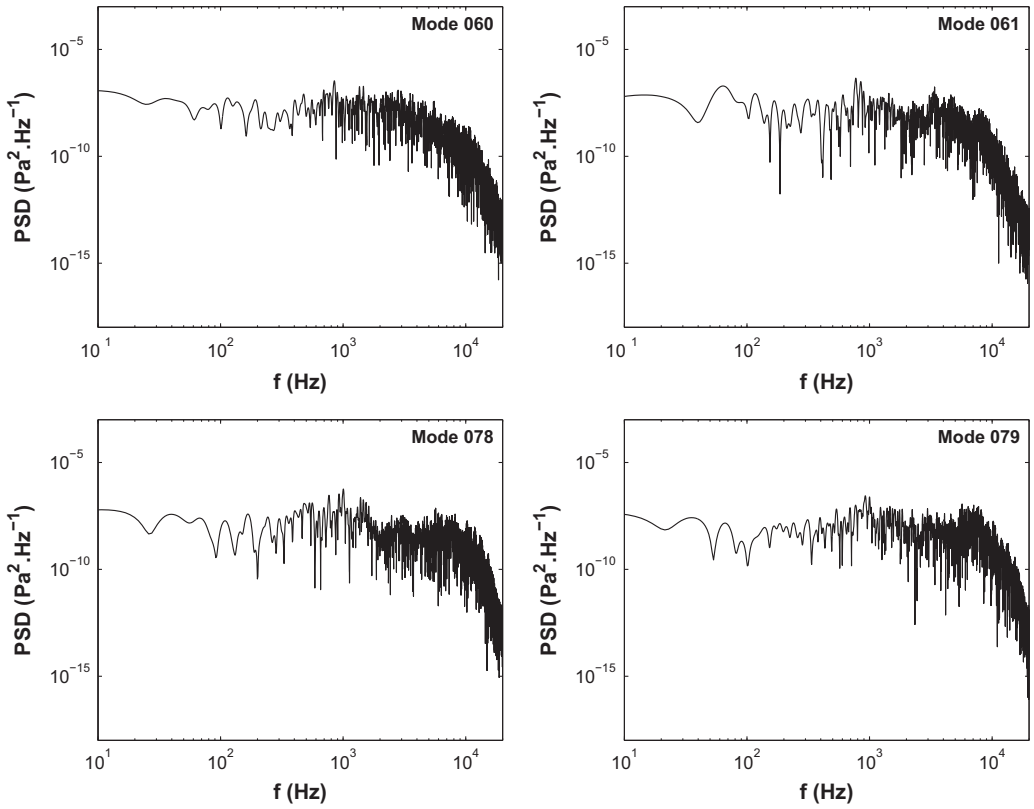

Fig. 27. PSD of temporal coefficient of higher POD modes.

turbulence intensity and $\tilde{r}$ is taken from a random number generator varying in the interval [0, 1]. This form is similar, from a dimensional point of view only, to the homogeneous ambient terms introduced by Spalart and Rumsey (2007) in order to sustains the turbulent kinetic energy level specified in the upstream conditions, which usually decays towards the body due to the dissipation rate:

$$\frac{\mathrm{D}k}{\mathrm{D}t} = P - \varepsilon + \frac{\partial}{\partial x_i}\left[\left(\nu + \frac{\nu_t}{\sigma_k}\right)\frac{\partial k}{\partial x_i}\right] + S_{\mathrm{POD}} \tag{11}$$

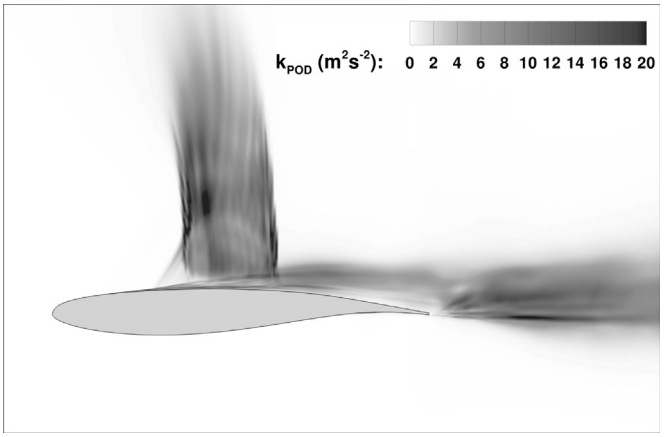

Fig. 28. Averaged turbulent kinetic enery field, k_{POD}, issued from fluctuating velocity reconstruction for higher-order modes 60–99.

$$\frac{D\varepsilon}{Dt}=\frac{\varepsilon}{k}(C_{\varepsilon 1}P-C_{\varepsilon 2}\varepsilon)+\frac{\partial}{\partial x_i}\left[\left(\nu+\frac{\nu_t}{\sigma_\varepsilon}\right)\frac{\partial \varepsilon}{\partial x_i}\right]+\frac{C_{\varepsilon 2}S_{POD}^2}{k_{amb}} \tag{12}$$

with

$$S_{POD}=\tilde{r}C_\mu(k_{amb}^2+k_{POD}^2)/\nu_{t\infty}, \tag{13}$$

and $\nu_t = C_\mu\ k^2/\varepsilon$ is the turbulent viscosity. $\nu_{t\infty}$ is the freestream turbulent viscosity.

In the present study, this source term is derived from the local-scale, higher-order POD modes. In Fig. 26, the higher-order POD shape modes, $\boldsymbol{\phi}_n(\mathbf{x})$, are maximum in the regions where the shearing rate is high (shear-layer and shock regions). In the present study, an order of the last 40 modes (from 60th to 99th) have this property, as shown in the previous section. This approach may be adapted for other cases. These POD modes are associated with the temporal coefficients by using the relation (6) in order to produce a reconstruction of the velocity components and to calculate a low-energy velocity scale, $\sqrt{u^2+v^2}$. This reconstruction used the whole snapshot sequence of 10 buffet periods as for the previous POD analysis. In this way, an averaged turbulent kinetic energy scale, k_{POD}, is calculated as: $k_{POD}=0.5\times(\overline{u^2}+\overline{v^2})$. As a first approximation, a *time-averaged* kinetic energy is evaluated. These equations *are time-dependent* and yield to a solution with temporal variation of the shear-layer as in Fig. 8. These source terms lead to a forcing of the turbulent stresses by means of the turbulence behaviour law and the turbulent viscosity. The new stresses act as an energy transfer from the stochastic small-scale modes to the higher ones.

As mentioned above, this stochastic forcing is simultaneously *localised* in the shear layer, in the wake and in the shock wave areas, thanks to the properties of the higher-order POD modes presented in the previous section, without contaminating the neighboring regions, which remain irrotational, as shown in the spatial distribution of k_{POD}, Fig. 28. The time-dependent evolution of these regions is taken into account. As will be discussed, the solution is now improved in respect of the shear-layer thinning.

Fig. 29 shows the divergence of the velocity vector at eight representative instants within the buffet period, according to the simulation including the stochastic forcing detailed above. A qualitative comparison with Fig. 8 shows a reduced shock-motion amplitude, which is in good agreement with the experiment. Furthermore, the shear layer and separated regions, which remain time-dependent, are thinner than in the previous case without stochastic forcing. These facts are quantified in Figs. 30, 32 and 33.

Fig. 30 shows a comparison of the mean surface pressure distribution between $k-\varepsilon$-OES and its variants with the experimental results. "*amb*" stands for the homogeneous ambient terms described in Spalart and Rumsey (2007), and "*IOES*" (I standing for "improved") refers to the modelling by stochastic forcing involving the k_{POD} field as discussed at the beginning of this section. The $k-\varepsilon$-OES without ambient terms provides a larger shock amplitude than in the experiment. The $k-\varepsilon$-OES with the homogeneous ambient terms provides an improvement in the shock-amplitude motion compared to the basic $k-\varepsilon$-OES simulation. In the IOES case, the pressure coefficient shows an even improved shock-motion amplitude where the shock-motion amplitude is large, as well as a better estimation of the pressure distribution in the region from the most downstream position of the shock to the trailing edge. This can be explained by the fact that the ambient terms and the stochastic forcing "add" a slight level of eddy viscosity in the OES modelling which is designed to reduce the eddy viscosity and to allow the instability development. Therefore, the instability development becomes slightly moderate by compensating the OES eddy-viscosity reduction thanks to the stochastic forcing. Moreover, the stochastic forcing improves the C_p tendency to form a more horizontal "plateau", upstream of the shock-motion area, as measured in the experiments. These improvements ensure a better estimation of the lift coefficient.

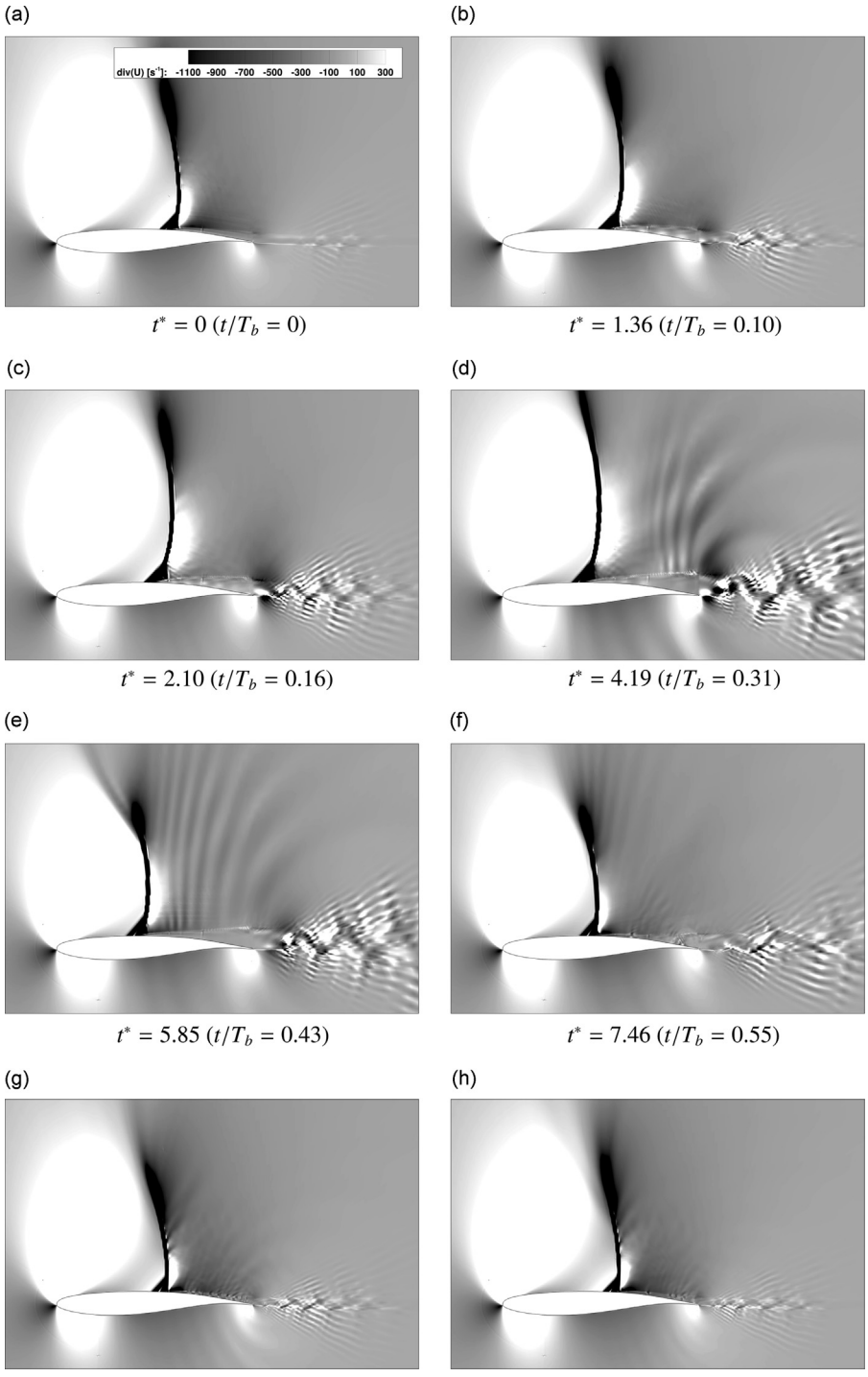

Fig. 29. Instantaneous fields of velocity divergence – application of the inhomogeneous stochastic forcing (T_b is the buffet period).

The TNT (Turbulent/Non-Turbulent) interface is localized where the vorticity gradient across the interface is maximum. The phase-averaged velocity and vorticity profiles derived from the $k-\varepsilon$-OES model, as well as from the IOES at the same phase, are compared in Figs. 32 and 33 at two positions: $x/C = 0.65$ and $x/C = 0.85$.

Fig. 31 shows the two locations where the phase-averaged velocity and vorticity profiles have been extracted at the same buffet phase to compare the stochastic forcing effects to the basic simulation.

Fig. 32 shows the comparison of these velocity profiles according to both approaches. It can be seen that the simulation with the forcing (IOES) leads to a significant thinning of the shear layer. This can also be observed in Fig. 33, where the two

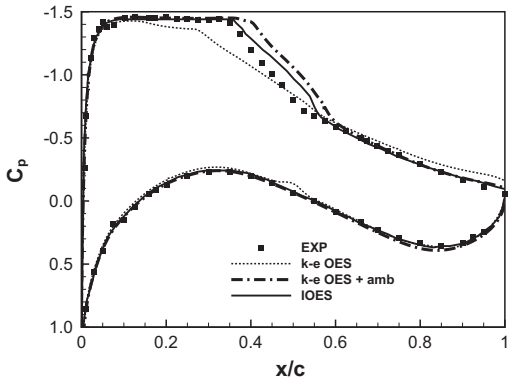

Fig. 30. Comparison of the mean surface pressure coefficient distribution between experiment, basic $k-\varepsilon$-OES modelling, $k-\varepsilon$-OES using the ambient terms of Spalart and Rumsey (2007): $k-\varepsilon$-OES + amb, stochastic forcing formulated in this study: IOES.

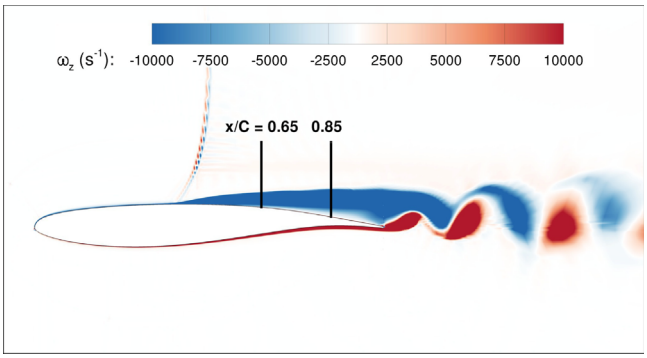

Fig. 31. Location of the phase-averaged velocity and vorticity profiles.

approaches are compared by means of the vorticity. The TNT interface, identified by a vorticity close to 0, is lowered by using the stochastic forcing. Its thickness is reduced by 30% at $x/C = 0.65$, and by 19% at $x/C = 0.85$, which has as a consequence the reduction of the drag, due to the reduction of the viscous region downstream of the shock. The present inhomogeneous forcing reproduces the blocking and thinning effect, similarly to the DNS results of Ishihara et al. (2015) regarding boundary-layer interface.

Fig. 34 left shows the velocity profile at the location $x/C = 0.85$, as well as the vorticity gradient profile at the same position (Fig. 34 right). Two *inflexion points* of the velocity profile are identified, corresponding to the change in sign of the vorticity gradient ($d\omega/dy = 0$). The existence of the inflexion points is associated indeed with the shear-layer instability development, illustrated in Fig. 29 as well as with the small series of Kelvin–Helmholtz vortices captured by the present simulation.

Following these results concerning the improved velocity profiles, a theoretical instability study can be carried out on the basis of the present velocity profiles in a future study, in order to accurately determine the critical shear rate beyond which the mentioned instabilities are amplified.

5. Conclusion

The present numerical study analyses in detail the flow physics of the transonic shock-wave, shear-layer and wake interaction around a supercritical airfoil at high Reynolds number (3 million), incidence of 3.5° and at a Mach number of 0.73. This set of physical parameters corresponds to the *onset* of the buffet instability, a challenge for the prediction of this instability appearance near the critical parameters by numerical simulation including turbulence modelling in the high-Reynolds number range. This study describes a new approach highlighting the dynamics of the transonic buffet in interaction with the near-wake von Kármán instability as well as with smaller-scale vortex structures in the separated shear layers, related to the Kelvin–Helmholtz instability.

This analysis is carried out by the Organized Eddy Simulation (OES) method, which resolves the organized coherent structures and models the random turbulence by adapted statistical modelling. This method has been improved in the present study to include stochastic forcing of smaller-scale vortex structures near the outer interfaces of the boundary layer, the shear layer and in the wake. Their effects are modelled as source terms in the turbulent kinetic energy and dissipation transport equations.

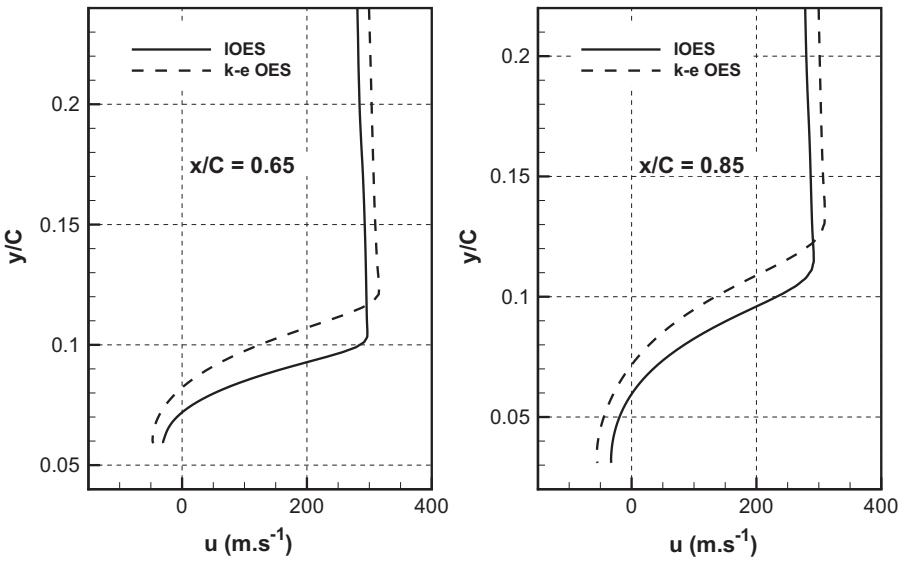

Fig. 32. Phase-averaged streamwise velocity profiles.

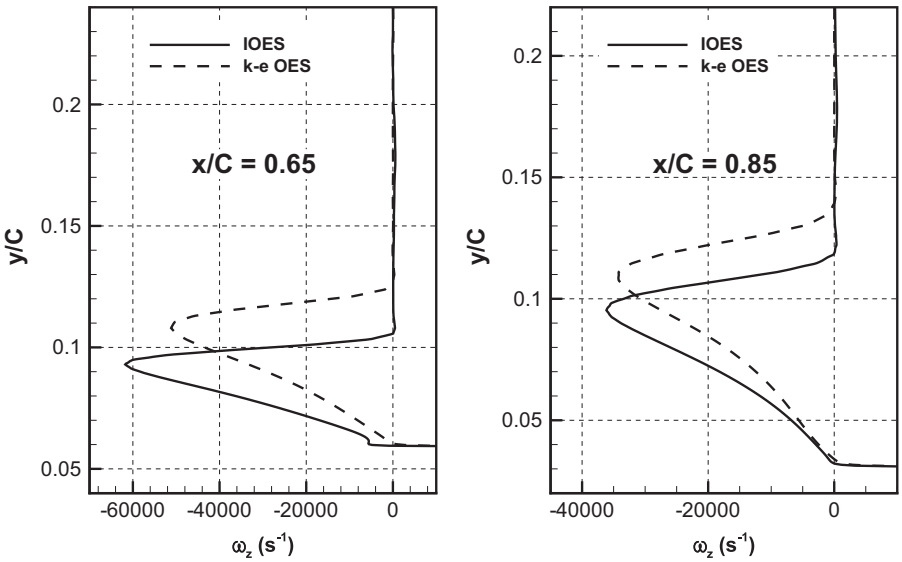

Fig. 33. Phase-averaged vorticity profiles.

By means of this modelling approach, the study contributes to complete experimental physical analysis of the transonic buffet, which was mainly interested in the shock motion and pressure-velocity distributions around the body and less in the interaction with the wake instabilities in the related literature. This study provides new results regarding the buffet interaction with the von Kármán mode and the smaller-scale vortex structures. The Proper Orthogonal Decomposition analysis has shown that this interaction creates an amplitude modulation of the buffet mode due to the von Kármán mode and vice-versa. The wavelet and autoregressive model analysis quantified a frequency modulation of the von Kármán instability due to the buffet. The predominant frequencies of these modes have been evaluated by spectral analysis and the interaction among them has been illustrated by the appearance of new frequencies in the energy spectrum, being combinations of the principal instability modes. Whereas the buffet mode is a well distinguished frequency peak in the spectrum, the von Kármán mode is characterized by a spectral 'bump' appearance around a frequency 33.3 times higher than the buffet frequency. The spectral analysis has shown the modification of the von Kármán mode 'bump' shape due to higher-order buffet harmonics and the amplification of the K–H instability peak of higher frequency.

Concerning these interactions, the POD analysis distinguished the shape modes involved in the formation of highly energetic coherent vortices and of the buffet dynamics from those of weaker energy involved in smaller-scale vortex structures appearing in the shear layers and influencing also the shock-motion area.

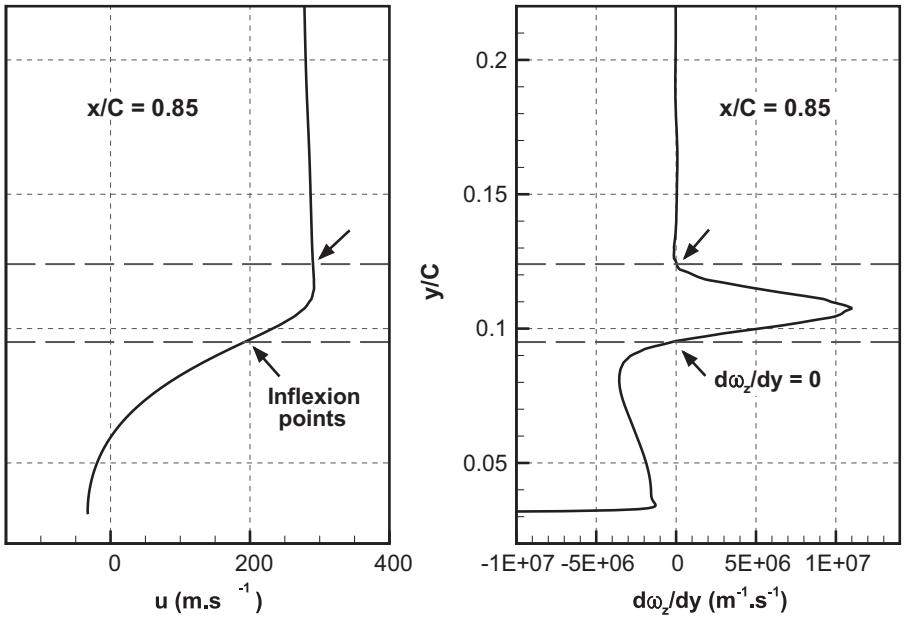

Fig. 34. IOES simulation: velocity (left) and vorticity gradient (right) profiles showing inflexion points outside and inside the upper thin shear layer interface.

Inspired from the POD reconstructions, an efficient inhomogeneous stochastic forcing has been built and applied as a source term in the turbulent kinetic energy and dissipation rate transport equations in the context of an improved OES (IOES) approach. By reconstructing the fluctuating velocity field corresponding to the higher-order POD modes, a kinetic energy fluctuation has been generated and employed in the stochastic forcing source terms. This forcing led to thinning of the turbulent/non-turbulent interfaces within the separated boundary layer and the shear layers.

An improved modelling of the shock amplitudes is obtained in comparison with experiments as well as a better physical representation of the instability regions and vortex structures around the body and in the wake. Furthermore, the present IOES method merits to be tested in 3D (although the buffet dynamics of a nominally 2D airfoil configuration are essentially two-dimensional) for a more accurate evaluation of the unsteady loads and pressure fluctuations generated by the fluid–structure interaction, a crucial issue in FIV (Flow-Induced Vibration) and aeroacoustics domains.

Acknowledgements

The authors acknowledge the financial and scientific support of the ATAAC (Advanced Turbulence Simulation for Aerodynamic Application Challenges) European Collaborative research program No. 233710, coordinated by DLR-Göttingen, by Dr. D. Schwamborn and including among the industrial partners Airbus, EADS, Dassault, Rolls Royce, Alenia and Eurocopter. The authors are grateful to the ONERA partner of this project for valuable scientific discussions and for the provision of a first numerical grid (S. Deck), as well as for the discussions on the impact of the two-dimensional character of the buffet around the wing, during the ATAAC project in the years 2009–2012. The computing time allocation was provided by the national computing centers CINES (Centre Informatique National de l'Enseignement Supérieur), CALMIP (Calcul en Midi-Pyrénées), IDRIS (Institut du Développement et des Ressources en Informatique Scientifique). This study partly used a computing allocation in the context of the PRACE-Tier1 and preparatory access supercomputing European initiative. The authors thank G. Harran and A. Sévrain for their scientific support concerning the dynamic systems analysis.

References

Alshabu, A., Olivier, H., 2008. Unsteady wave propagation phenomena on a supercritical airfoil. AIAA Journal 46 (8), 2066–2073.

Aubry, N., Guyonnet, R., Lima, R., 1991. Spatio-temporal analysis of complex signals: theory and applications. Journal of Statistical Physics 64 (3-4), 683–739.

Barbut, G., Braza, M., Hoarau, Y., Barakos, G., Sévrain, A., Vos, J.B., 2010. Prediction of transonic buffet around a wing with flap. In: Progress in Hybrid RANS-LES Modelling, Notes on Numerical Fluid Mechanics and Multidisciplinary Design, vol. 111. Springer, Gdansk, Poland. pp. 191–204.

Bodenschatz, E., Eckert, M., 2011. Prandtl and the Göttingen school. In: Davidson, P.A., et al. (Eds.), A Voyage Through Turbulence, Cambridge University Press, Cambridge.

Bouhadji, A., 1998. Analyse physique par simulation numérique de phénomènes de transition bi- et tridimensionnels dans l'écoulement compressible, visqueux autour d'une aile d'avion (Ph.D. thesis). INPT.

Bouhadji, A., Braza, M., 2003a. Organised modes and shock–vortex interaction in unsteady viscous transonic flows around an aerofoil. Part I. Mach number effect. Journal of Computers and Fluids 32 (9), 1233–1260.
Bouhadji, A., Braza, M., 2003b. Organised modes and shock–vortex interaction in unsteady viscous transonic flows around an aerofoil. Part II. Reynolds number effect. Journal of Computers and Fluids 32 (9), 1261–1281.
Bourdet, S., Bouhadji, A., Braza, M., Thiele, F., 2003. Direct numerical simulation of the three-dimensional transition to turbulence in the transonic flow around a wing. Flow, Turbulence and Combustion 71 (1–4), 203–220.
Bourgoyne, D.A., Ceccio, S.L., Dowling, D.R., 2005. Vortex shedding from a hydrofoil at high Reynolds number. Journal of Fluid Mechanics 531, 293–324.
Bourguet, R., Braza, M., Harran, G., El Akoury, R., 2008. Anisotropic organised eddy simulation for the prediction of non-equilibrium turbulent flows around bodies. Journal of Fluids and Structures 24 (8), 1240–1251.
Braza, M., 2011. NACA0012 with Aileron. In: Doerffer, P., Hirsch, C., Dussauge, J.-P., Babinsky, H., Barakos, G.N. (Eds.), Unsteady Effects of Shock Wave Induced Separation, Notes on Numerical Fluid Mechanics and Multidisciplinary Design, vol. 114. Springer, Berlin, Heidelberg, pp. 101–131.
Braza, M., Faghani, D., Persillon, H., 2001. Successive stages and the role of natural vortex dislocations in three-dimensional wake transition. Journal of Fluid Mechanics 439, 1–41.
Braza, M., Perrin, R., Hoarau, Y., 2006. Turbulence properties in the cylinder wake at high Reynolds number. Journal of Fluids and Structures 22 (6–7), 757–771.
Brunet, V., 2003. Computational study of buffet phenomenon with unsteady RANS equations. In: 21st AIAA Applied Aerodynamics Conference. Orlando, FL, USA, AIAA 2003-3679, 23–26 June.
Brunet, V., Deck, S., Molton, P., Thiery, M., 2005. A complete experimental and numerical study of the buffet phenomenon over the OAT15A airfoil. In: 40th Colloque d'Aérodynamique Appliquée, 21–23 March, Toulouse, France.
Deck, S., 2005. Numerical computation of transonic buffet over a supercritical airfoil. AIAA Journal 43 (7), 1556–1566.
Dritschel, D., Haynes, P., Juckes, M., Shepherd, T., 1991. The stability of a two-dimensional vorticity element under uniform strain. Journal of Fluid Mechanics 230, 647–665.
Duncan, W.J., Ellis, L., Scruton, C., 1932. First report on the general investigation of tail buffeting. Aeronaut. Research. Com. R. & M. 1457, part I.
Durbin, J., 1960. The fitting of time series models. Review of the International Statistical Institute 28, 233–243.
Eames, I., Flor, J., 2011. New developments in understanding interfacial processes in turbulent flows. Philosophical Transactions of the Royal Society A: Mathematical, Physical and Engineering Sciences 369 (1937), 702–705.
Edwards, J.R., Chandra, S., 1996. Comparison of eddy viscosity-transport turbulence models for three-dimensional, shock-separated flowfields. AIAA Journal 34 (9), 756–763.
El Akoury, R., Braza, M., Perrin, R., Harran, G., Hoarau, Y., 2008. The three-dimensional transition in the flow around a rotating cylinder. Journal of Fluid Mechanics 607, 1–11.
Fu, S., Haase, W., Peng, S.H., Schwamborn, D. (Eds.), 2012. Progress in Hybrid RANS-LES Modelling, Notes on Numerical Fluid Mechanics and Multidisciplinary Design, vol. 117, Springer, Beijing, China.
Fung, Y.C., 2002. An Introduction to the Theory of Aeroelasticity. Dover, Schlieren Picture Page 313 by D. W. Holder, National Physical Laboratory, England.
Grossi, F., 2010. Simulation numérique et analyse physique du tremblement transsonique d'un profil supercritique par approche de modélisation de la turbulence statistique avancée (Master's thesis). IMFT.
Grossi, F., 2014. Physics and Modeling of Unsteady Shock Wave/Boundary Layer Interactions Over Transonic Airfoils by Numerical Simulation (Ph.D. thesis). INP Toulouse.
Grossi, F., Braza, M., Hoarau, Y., 2011. Simulation numérique et analyse physique du tremblement transsonique d'un profil supercritique à Reynolds élevé. 20 th Congrès Français de Mécanique, 29 August–2 September.
Grossi, F., Braza, M., Hoarau, Y., 2012a. Delayed detached-eddy simulation of the transonic flow around a supercritical airfoil in the buffet regime. In: Progress in Hybrid RANS-LES Modelling. Notes on Numerical Fluid Mechanics and Multidisciplinary Design, vol. 117. Springer, Beijing, China, pp. 369–378.
Grossi, F., Braza, M., Hoarau, Y., 2014. Prediction of transonic buffet by delayed detached-eddy simulation. AIAA Journal 52, 2300–2312.
Grossi, F., Szubert, D., Braza, M., Sevrain, A., Hoarau, Y., 2012b. Numerical simulation and turbulence modelling of the transonic buffet over a supercritical airfoil at high Reynolds number. In: Proceedings of the ETMM9 9th International ERCOFTAC Symposium on Engineering Turbulence Modelling and Measurements. Thessaloniki, Greece, 6–8 June.
Grossmann, A., Morlet, J., 1984. Decomposition of Hardy functions into square integrable wavelets of constant shape. SIAM Journal on Mathematical Analysis 15 (4), 723–736.
Guzmán, A.M., Amon, C.H., 1994. Transition to chaos in converging-diverging channel flows: Ruelle-Takens-Newhouse scenario. Physics of Fluids 6.
Haase, W., Braza, M., Revell, A. (Eds.), 2009. DESider – A European Effort on Hybrid RANS-LES Modelling: Results of the European-Union Funded Project, 2004-2007, Notes on Numerical Fluid Mechanics and Multidisciplinary Design, vol. 103, Springer.
Hoarau, Y., 2002. Analyse physique par simulation numérique et modélisation des écoulements décollés instationnaires autour de surfaces portantes (Ph.D. thesis). INPT.
Holzner, M., Liberzon, A., Nikitin, N., Lüthi, B., Kinzelbach, W., Tsinober, A., 2008. A Lagrangian investigation of the small-scale features of turbulent entrainment through particle tracking and direct numerical simulation. Journal of Fluid Mechanics 598, 465–475.
Hunt, J., Richards, K., 1984. Stratified airflow over one or two hills. In: Kaplan, H., Dinar, N. (Eds.), Boundary Layer Structure, Springer, Zichron Yaacov, Israel, pp. 223–259.
Hunt, J. C.R., Eames, I., Westerweel, J., 2008. Vortical interactions with interfacial shear layers. In: Kaneda, Y. (Ed.), IUTAM Symposium on Computational Physics and New Perspectives in Turbulence, IUTAM Bookseries, vol. 4, Springer, Nagoya, Japan, pp. 331–338.
Hunt, J.C.R., Ishihara, T., Worth, N.A., Kaneda, Y., 2014. Thin shear layer structures in high Reynolds number turbulence. Flow, Turbulence and Combustion 92 (3), 607–649.
Ishihara, T., Ogasawara, H., Hunt, J.C.R., 2015. Analysis of conditional statistics obtained near the turbulent/non-turbulent interface of turbulent boundary layer. Journal of Fluids and Structures 53, 50–57. http://dx.doi.org/10.1016/j.jfluidstructs.2014.10.008.
Jacquin, L., Molton, P., Deck, S., Maury, B., Soulevant, D., 2005. An experimental study of shock oscillation over a transonic supercritical profile. In: 35th AIAA Fluid Dynamics Conference and Exhibit, Toronto, Ontario, Canada, AIAA 2005-4902, 6–9 June.
Jacquin, L., Molton, P., Deck, S., Maury, B., Soulevant, D., 2009. Experimental study of shock oscillation over a transonic supercritical profile. AIAA Journal 47 (9), 1985–1994.
Jimenez-Garcia, A., 2012. Etude de l'interaction tremblement transsonique – instabilité de von Kármán à l'aide d'une plaque de bord de fuite par approche de modélisation de la turbulence statistique avancée (Master's thesis). IMFT.
Landau, L.D., 1944. On the problem of turbulence. Comptes Rendus Academic Sciences URSS 44 (31), 1–314.
Lee, B.H.K., 1990. Oscillatory shock motion caused by transonic shock boundary-layer interaction. AIAA Journal 28 (5), 942–944.
Levy Jr., L.L., 1978. Experimental and computational steady and unsteady transonic flows about a thick airfoil. AIAA Journal 16 (6), 564–572.
Martinat, G., Braza, M., Hoarau, Y., Harran, G., 2008. Turbulence modelling of the flow past a pitching NACA0012 airfoil at 10^5 and 10^6 Reynolds numbers. Journal of Fluids and Structures 24 (8), 1294–1303.
McDevitt, J.B., Levy Jr., L.L., Deiwert, G.S., 1976. Transonic flow about a thick circular-arc airfoil. AIAA Journal 14 (5), 606–613.
Menter, F., Egorov, Y., 2005. A scale-adaptive simulation model using two-equation models. In: 43rd AIAA Aerospace Sciences Meeting and Exhibit, AIAA Paper 2005–1095, 10–13 January.
Menter, F., Kuntz, M., Bender, R., 2003. A scale-adaptive simulation model for turbulent flow prediction. In: 41st AIAA Aerospace Sciences Meeting and Exhibit, AIAA paper 2003–0767, 6–9 January .

Menter, F.R., 1994. Two-equation eddy-viscosity turbulence models for engineering applications. AIAA Journal 32 (8), 1598–1605.
Newhouse, S., Ruelle, D., Takens, F., 1978. Occurrence of strange axiom A attractors near quasi periodic flows on T_m, $m \leq 3$. Communications in Mathematical Physics 64 (1), 35–40.
Perrin, R., Braza, M., Cid, E., Cazin, S., Moradei, F., Barthet, A., Sevrain, A., Hoarau, Y., 2006. Near-wake turbulence properties in the high Reynolds number incompressible flow around a circular cylinder measured by two- and three-component PIV. Flow, Turbulence and Combustion 77 (1–4), 185–204.
Roe, P.L., 1981. Approximate Riemann solvers, parameter vectors, and difference schemes. Journal of Computational Physics 43 (2), 357–372.
Rung, T., Bunge, U., Schatz, M., Thiele, F., 2003. Restatement of the Spalart–Allmaras eddy-viscosity model in strain-adaptive formulation. AIAA Journal 41 (7), 1396–1399.
Seegmiller, H.L., Marvin, J.G., Levy Jr., L.L., 1978. Steady and unsteady transonic flow. AIAA Journal 16 (12), 1262–1270.
Shur, M., Strelets, M., Zaikov, L., Gulyaev, A., Kozlov, V., Secundov, A., 1995. Comparative numerical testing of one- and two-equation turbulence models for flows with separation and reattachement. In: 33rd Aerospace Sciences Meeting and Exhibit, Reno, NV, USA, AIAA 95-0863, 9–12 January.
Sirovich, L., 1990. Turbulence and the dynamics of coherent structures, Parts I, II & III. Quarterly Journal of Applied Mathematics XLV (3), 561–582.
Spalart, P.R., 2000. Trends in turbulence treatments. In: Fluids 2000 Conference and Exhibit, Denver, CO, USA, AIAA Paper 2000–2306, 19–22 June.
Spalart, P.R., Allmaras, S.R., 1994. A one-equation turbulence model for aerodynamic flows. Recherche Aerospatiale 1, 5–21.
Spalart, P.R., Rumsey, C.L., 2007. Effective inflow conditions for turbulence models in aerodynamic calculations. AIAA Journal 45 (10), 2544–2553.
Taveira, R.R., da Silva, C.B., 2014. Characteristics of the viscous superlayer in shear free turbulence and in planar turbulent jets. Physics of Fluids 26 (2), 021702.
Thiery, M., Coustols, E., 2005. URANS computations of shock-induced oscillations over 2D rigid airfoils: Influence of test section geometry. Flow, Turbulence and Combustion 74 (4), 331–354.
van Leer, B., 1979. Towards the ultimate conservative difference scheme. V. A second-order sequel to Godunov's method. Journal of Computational Physics 32 (1), 101–136.
Vos, J.B., Rizzi, A.W., Corjon, A., Chaput, E., Soinne, E., 1998. Recent advances in aerodynamics inside the NSMB (Navier Stokes Multi Block) consortium. In: 36th AIAA Aerospace Sciences Meeting and Exhibit, Reno, NV, USA, AIAA Paper 98–0225, 12–15 January.
Welch, P.D., 1967. The use of fast fourier transform for the estimation of power spectra: a method based on time averaging over short, modified periodograms. IEEE Transactions on Audio and Electroacoustics 15 (2), 70–73.
Westerweel, J., Fukushima, C., Pedersen, J.M., Hunt, J.C.R., 2009. Momentum and scalar transport at the turbulent/non-turbulent interface of a jet. Journal of Fluid Mechanics 631, 199–230.